CERES S-NPP VIIRS Edition1A SSF Cloud Properties - Accuracy and Validation

This section discusses the spectral radiances and cloud products included in the **SSF** data set version **S-NPP VIIRS Edition 1A**. Additional information is in the Description/Abstract Guide. The goal of CERES is to provide a long-term consistently analyzed cloud and radiation dataset. CERES employs radiance data taken from different platforms with a variety of sensors, including imagers used to retrieve cloud properties. Thus, it is essential to apply the same algorithms to the imager data as much as possible to obtain cross-platform consistency, as well as long term stability in the various retrieved parameters. To accomplish this, a set of algorithms was developed based on the CERES Edition 2 cloud processing system (Minnis et al., 2008a, 2011a) and adapted to apply to both geostationary (GEO) (Minnis et al., 2008b) and other low-Earth-orbiting satellite imager data, particularly the MODerate-resolution Imaging Spectroradiometer (MODIS) and the Visible/Infrared Imaging Radiometer Suite (VIIRS). The algorithms were upgraded for CERES MODIS Edition 4. For detailed descriptions of the Edition-4 algorithms, see Trepte et al. (2019) for the cloud mask and Minnis et al. (2021) for the retrievals. Changes to those algorithms for CERES SNPP VIIRS Ed1a are discussed here along with an evaluation of the quality and pertinent characteristics of the data.

For brevity, acronyms corresponding to the CERES version are used instead of writing out the version each time it is referenced. The generic acronym ABCD is used where A is the project that developed and applied the version, B is instrument, C is the version number or edition, and D is the satellite. Each of these items can be represented by more than one character, if needed, and D can be omitted when discussing algorithms or results common to more than one satellite. Thus, CERES MODIS Edition 4 is used for MODIS on Terra and Aqua, and CM4A is CM4 for Aqua only. The CERES SNPP VIIRS Ed1a is denoted as CV1S, where S denotes SNPP. For comparisons, a given parameter X from CM4A or CV1S is denoted as X(M) or X(V), respectively.

Cloud products in the CERES SNPP SSF are the result of convolving the values for the clear-sky and cloudy parameters derived for each 750-m (375 m) VIIRS pixel sampled every eighth pixel and every other scan line (see Convolution Process) to give an effective resolution of 6 x 1.5 km (~9 km^2) to reduce processing time and data storage. Six primary radiances taken at 0.64 (visible, VIS), 1.24 (near infrared 1, NIR1), 1.61 (near infrared 2, NIR2), 3.74 (shortwave infrared, SIR), 10.8 (infrared, IR), and 12.0 (split-window channel, SWC) μm, channels 1, 5, 7, 20, 31, and 32, respectively, are used for each VIIRS pixel. VIIRS 0.49, 0.86, 1.38, and 8.55-μm channels are also used for cloud detection. The channels, wavelength λ, usage, and comparability with MODIS are listed in Table 1 along with the VIIRS

Table 1. SPECTRAL CHANNELS USED IN CERES CLOUD RETRIEVALS

| CERES Channel #	MODIS Channel #	VIIRS Channel #	MODIS Central Wavelength (μm)	VIIRS Central Wavelength (μm)	MODIS CM4	VIIRS CV1S	Name
1	1	I1	0.65	0.64	1,2	1,2	VIS
2a	6	I3	1.61	1.61	-	1,2	NIR
2b	7	M11	2.13	2.26	1,2	-	NIR
3	20	I4	3.78	3.74	1,2	1,2	SIR
4	31	M15	11.0	10.8	1,2	1,2	IRW
5	32	M16	12.0	12.0	1,2	1,2	SPW
6	29	M14	8.55	8.55	1,2	1,2	IRP
7	5	M8	1.24	1.24	1,2	1,2	SNI
8	3	M3	0.47	0.49	1	1	
9	26	M9	1.38	1.38	1	1	
10	2	I2	0.86	0.86	1	1	VEG
11	27		6.71	N/A	1	N/A	WV
12	33		13.3	N/A	1,2	N/A	CO2

Use Key: 1 – mask   2 – retrieval
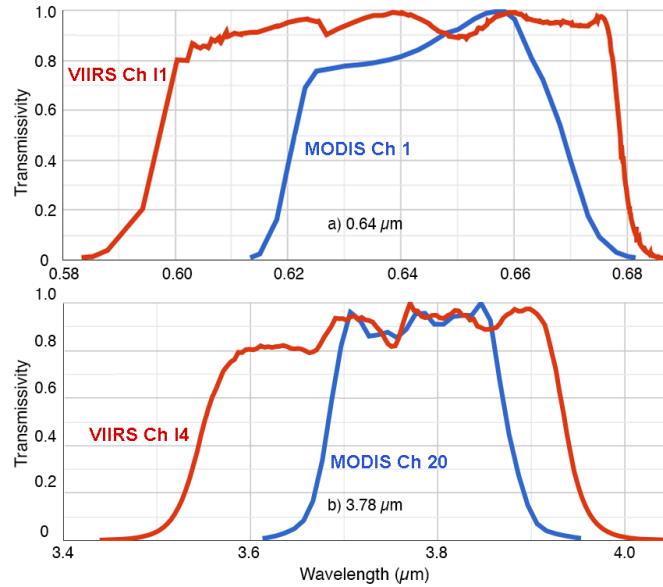
Figure 1. Spectral response functions for CERES channels (a) 1 and (b) 3 used in cloud detection and retrieval algorithms.

channel numbers. Those starting with "I" have a nominal 375-m resolution, half of the "M" channels' resolution. The CERES channel numbers (n) are also shown as these provide a common channel reference for all satellites used in CERES processing. As indicated in Table 1, the CV1S cloud mask and retrieval algorithms use 10 and 7 VIIRS channels, respectively, compared to 12 and 8 for CM4 cloud processing. The cloud products rely on accurately calibrated imager radiances. VIIRS Ed1 input radiances were provided by the NASA VIIRS Land Science Investigator-led Processing System Collection 1 product Level 1B geo-located and calibrated radiance data. These data were calibrated using the approach of Xiong et al (2014), who discuss the initial performance of the sensors. The VIIRS calibrations were updated beginning January 2016, resulting in an increase in the average VIS reflectance.

While the common channels are similar, there are instrument-to-instrument differences that must be resolved to maximize consistency. For example, Figure 1 shows the spectral response functions (SRF) for the Aqua MODIS (red) and SNPP VIIRS (blue) channels corresponding to CERES channels 1 (Figure 1a) and 3 (Figure 1b). The VIIRS wavebands are broader than and encompass their MODIS counterparts with centers shifted slightly to shorter wavelengths. These discrepancies affect the spectral solar constants, the corrections for atmospheric absorption and scattering, and, in some cases, the optical properties assumed for the cloud retrievals. Changes to the mask and retrieval algorithms were made to account for those differences.

In addition to its higher resolution, the VIIRS pixel sizes vary minimally with increasing scan angle (SA) or viewing zenith angle (VZA), unlike MODIS pixels. Combinations of sub-pixels are used to produce the operational pixels recorded by VIIRS. The number of sub-pixels used for each pixel decreases at SA = 32° and again at 43°, so that instead of the area of each pixel rising monotonically with VZA, it suddenly decreases at SA =32° and again at 43° (Lee et al., 2006). Thus, while the MODIS pixel size increases by a factor of 5 at SA = 50°, the VIIRS pixel size has risen by less than 25%. This characteristic can possibly can give rise to additional differences between VIIRS and MODIS cloud property retrievals.

Scene Identification (Scene-ID) or Cloud Mask

The radiances, in the form of reflectances (ρ_λ)and brightness temperatures (BT_n), are used to classify each VIIRS pixel as clear, cloudy, bad data, or no retrieval. Brightness temperature differences (BTDn1,n2) and reflectance ratios ($\rho_{\lambda 1}/\rho_{\lambda 2}$) are also used in the scene ID process. Each clear or cloudy pixel is categorized as weak or strong indicating the degree of confidence. Clear pixels can have an additional classifier: snow, aerosol, smoke, fire, glint, or shadow. Cloudy pixels can also have a glint sub-classification meaning that they were detected at angles favorable for the viewing of specular reflection from the surface. Estimates of surface skin temperature and atmospheric profiles of ozone, and humidity from the Global Modeling and Assimilation Office (GMAO) Goddard Earth Observing System Model Version 5.41 (GMAO-G541), elevation, and one of the 19 surface types (CERES Surface Type IDs) are also associated

with each VIIRS pixel. Lacking an equivalent to MODIS channel 7 (VIIRS M11 has distinctly different indices of refraction for water), VIIRS channel I3 (1.61 μm) is being used in its place. The 1.60-μm channel is the waveband originally preferred for CERES retrievals and daytime ice/snow detection. Absent the CO2 and WV channels on VIIRS, various adjustments were made to the scene ID and retrieval algorithms. The following remarks summarize changes in the cloud mask for CV1S relative to the scene-ID methods used for CM4.

- Daytime non-polar
  - All tests using $\rho_{2.1}$ were replaced with $\rho_{1.6}$, and the thresholds adjusted for CM4-CV1S equivalency
  - Refined sun-glint detection in cloudy areas.
  - Tests using channel 11 or 12 eliminated.
- Nighttime non-polar
  - Eliminated or replaced tests using channel 11 or 12. Adjusted thresholds to account for changes.
- Daytime Polar
  - All tests using $\rho_{2.1}$ were replaced with $\rho_{1.6}$, and the thresholds adjusted for CM4-CV1S equivalency
  - For super cold plateau, tests using BTD_{1112} and BTD_{114} were replaced with new tests using BTD_{45} or removed.
- Nighttime Polar
  - Tests using channels 11 and 12 were replaced with new tests using BTD_{45}, BTD_{35}, BTD_{34}, T_{cs}, and T_4.
- Twilight Polar: Same as daytime polar

Cloud Property Retrievals

The following parameters are determined for each cloudy pixel: phase (ice or water), VIS optical depth (over snow-covered surfaces, the SNI channel replaces the VIS channel), IR emissivity, cloud water path *CWP*, water droplet or ice crystal effective radius R_e at three wavelengths (3.7, 1.6 and 1.24 μm), cloud-top, effective, and base pressure (p_t p_c and p_b respectively), cloud-top, effective and base height (Z_t, Z_c and Z_b respectively), cloud-top, effective, and base temperature (T_t, T_c, and T_b respectively), cloud-top height (pressure and temperature) from the channel 4 – channel 5 brightness temperature difference, BTD_{45}, retrieval of Z_{C45} (P_{C45} and T_{C45}), multilayer (ML) identification, upper-layer (UL) cloud-top height (pressure and temperature), upper-layer effective ice crystal radius R_e at two wavelengths (3.7 and 1.6 μm), lower-layer (LL) cloud-top height (pressure and temperature), lower-layer effective water droplet radius R_e at two wavelengths (3.7 and 1.6 μm). While all parameters are given a value or retain a default value and may be used in the construction of the SSF, individual pixel values are retained for the parameters listed in Table 2. These are saved for use in validation and other analyses of cloud properties. No values are assigned to cloudy pixels having no retrievals. No properties could be

Table 2. Single pixel parameters saved for each VIIRS pixel and provided along with other variables for construction of SSF.

Latitude, longitude (°)	BTM cloud top altitude, Z_{CO2} (km)
Solar zenith angle, SZA (°)	BTM multilayer upper cloud top altitude, Z_{UL} (km)
Viewing zenith angle, VZA (°)	BTM multilayer lower cloud top altitude, Z_{LL} (km)
Relative azimuth angle, RAA (°)	BTM multilayer upper cloud ice R_e: R_{UL} (μm)
CERES channel 1 and 2a reflectances: ρ_1, ρ_{2a}	BTM multilayer lower cloud water R_e: R_{LL} (μm)
CERES channel 3, 4, and 5 temperatures: T_3, T_4 T_5 (K)	BTM multilayer upper cloud IR optical depth: τ_{UL}
Cloud droplet or ice crystal effective radius at 3.8 μm, R_e (μm)	BTM multilayer lower cloud IR optical depth: τ_{LL}
Cloud optical depth, τ	BTM multilayer detection index
Cloud water path (gm^{-2}), CWP	Standard CERES BTD_{45} multilayer detection index
Cloud effective, top, and base altitude, Z_e, Z_t, Z_b (km)	Pavolonis multilayer detection index
Cloud effective temperature, T_c (K)	IGBP surface type (1-18)
Cloud Mask Value	Snow map index (0 = no snow; 1 = snow)
Cloud Mask Clear Category	Ice map percentage (%)
Cloud Mask Cloud Category	SINT_VISST flag
Cloud Particle Phase	Cloud droplet/ice crystal effective radius at 1.24 μm, R_e (μm)
	Cloud droplet/ice crystal effective radius at 1.61 μm, R_e (μm)

retrieved for ~1.0 and ~2.5% of the detected cloudy pixels over ocean and land, respectively, during the day for a total of ~1.5%, almost a factor of 2 increase from CM4. At night, the number of no-retrievals drops to ~0.2% of the total number of pixels classified as cloudy, the fraction found with CM4.

Normally, the cloud phase, temperature, effective particle size and optical depth are computed using the VIS-IR-NIR-SWC Technique (VISST), which matches model estimates of radiances from clouds with the observations (Minnis et al. 2011a). The VIS channel is primarily used to estimate τ, the IR channel is for T_c, the SIR channel is used for the particle size, and the SWC is used to help the phase selection. Cloud height and pressure are found by matching T_c to an altitude in the GMAO-G541 vertical profile of temperature for the pixel location and time. If the underlying surface is determined to be snow- or ice-covered either from the snow-ice maps or from identification of nearby pixels as clear snow, then the SIR-IR- NIR1 Technique (SINT) is applied (Minnis et al. 2011a, 2021). The SINT uses the SNI channel to compute the VIS optical depth.

All ice crystal reflectance lookup tables (LUT) for the 0.6, 3.7, 1.6, and 1.2 μm channels used in CV1S are based on radiative transfer computations using hexagonal ice columns with roughened surfaces having the normalized roughness parameter set equal to 1.0 (Yang et al. 2008). These are the same models used for CM4, except the calculations were performed employing a discrete-ordinates method instead of the adding-doubling technique used previously.

The water droplet reflectance LUTs used in CV1S are the same as those in CM4, except that new LUTs were computed for the 0.65, 1.24, 1.6, and 3.7-μm channels using the discrete ordinates method and a different way to calculate the average index of refraction. For CM4, the indices of refraction for each band were assumed to be equal to the value at the central wavelength (Minnis et al., 1998). For the CV1S computations, the mean index was calculated by convolving the indices of refraction for each of the discrete band subsections with the spectral filter function (e.g., Figure 1), and the incoming solar irradiance. The new LUTs tend to yield a smaller value of R_e, but have minimal impact on τ. Corrections for atmospheric absorption use radiative transfer calculations, as in Minnis et al. (2011a, 2021), employing the correlated k-distribution method with the absorption coefficients computed for the spectral response functions of the various channels.

The Modified CO_2-Absorption Technique (MCAT) developed by Chang et al. (2010a) utilizes CERES channels 4 (10.8 μm) and 12 (13.3. μm) to estimate the cloud and background temperatures simultaneously, providing alternate cloud temperature, height, and pressures for certain pixels. As VIIRS lacks channel 12, the algorithm was modified to use channel 4 and the brightness temperature difference between channels 4 and 5 (12.0 μm). This algorithm is designated as the brightness temperature-difference method (BTM). In addition to providing an alternative estimate of Z_t, it replaces the MCAT in the experimental multilayer (ML) cloud detection and retrieval algorithm (see Chang et al., 2010b,c). The associated parameters are denoted with BTM in Table 2.

Standard Cloud Parameters

Validation relies on direct comparisons of CV1S cloud properties with ground truth data and other satellites, and especially on consistency with Aqua CM4 (CM4A) data, which have been compared with many other reference datasets. The results have also been averaged for various surface types and angular ranges to determine any systematic variability.

Inter-platform consistency and changes relative to CM4A

Consistency with CM4A is a critical goal for CERES as the VIIRS products are expected to completely replace those from MODIS in the future and, therefore, should be as much like them as possible.

Cloud amount:

The distributions of 2013 mean cloud fraction, CF, from CV1S and their regional differences with CM4A are plotted in Figure 2. The global patterns in CF during day (Figure 2a) and night (Figure 2b) are very similar, except in the polar regions. Moreover, in nonpolar areas, CF generally appears to be greater at night. Overall, the CV1S global mean cloud fraction increases by 0.02 from day to night, despite the nearly 0.03 drop in polar cloudiness. During the daytime, CF(V) is generally about 0.01-0.02 less than CF(M) (Figure 2c), except over some desert areas and some tropical littorals. The non-polar positive differences occur in areas with seasonal dust and smoke outbreaks. The greatest negative differences are in trade cumulus areas and central Greenland. On average, the daytime CM4A CF is 0.013 greater than the CV1S cloud fraction. At night (Figure 2d), the differences over tropical ocean and large portions of the permanent sea ice and snow areas are strongly negative, while CF(V) exceeds CF(M) over many land areas, particularly where desert and tundra prevail. In the nocturnal global mean, CF(V) is 0.025 less than CF(M). Over the polar regions, the large negative and positive regional differences cancel to some degree but the mean difference is still significant at -0.020. The wide regional variability and increased negative difference in those cold regions at night are likely due to the lack of CERES channels 11 and 12 on the VIIRS and the reduced sensitivity in the VIIRS I4 band at very low temperatures relative to that of the MODIS channel 20.
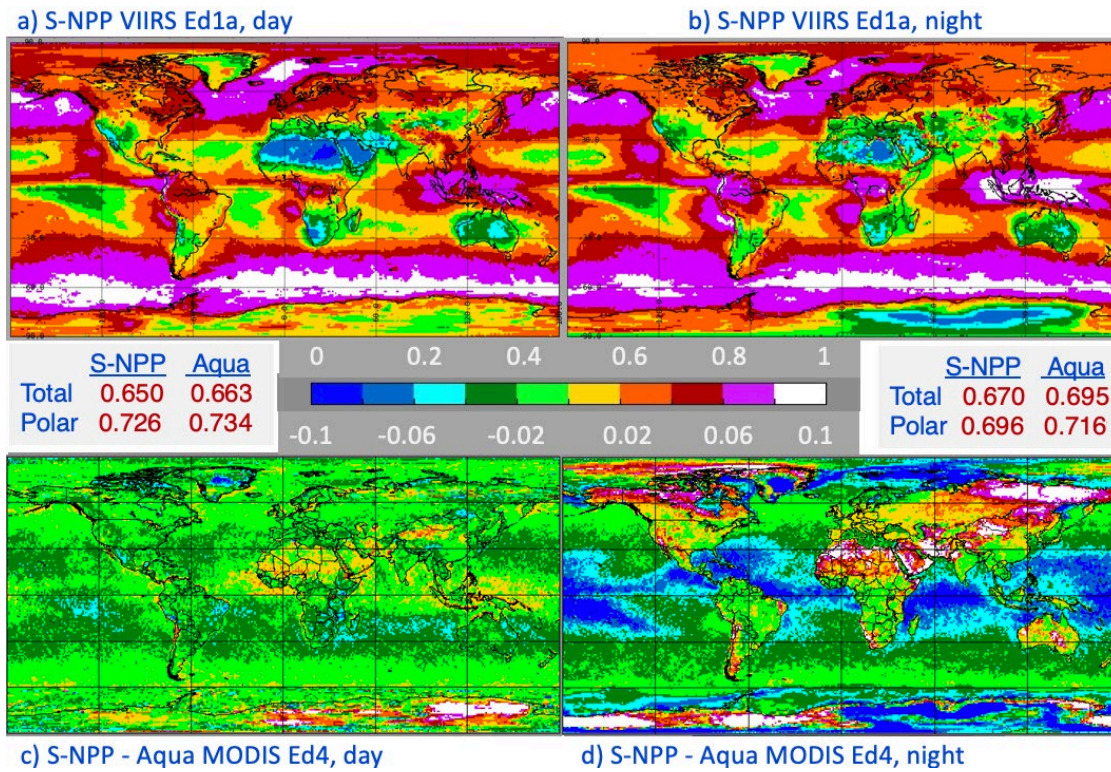
4

Figure 2. Mean 2013 cloud fractions from CV1S for (a) day and (b) night with the differences between CV1S and CM4 for (c) day and (d) night.

Figure 3 shows the time series of daytime cloud fraction from CM4A (blue) and CV1S (green) as 12-month running means between 2012 and 2020. Note the different scales in each plot. In nonpolar regions (Figure 3a), the average difference between the two datasets is relatively constant around -0.015. The trends for these 9 years are -0.7 and -0.5 %/decade for CV1S and CM4A, respectively. Over polar areas, the CF differences vary between -0.004 to -0.014 (Figure 3b). Here, the CF trends are positive at 1.6 and 1.5%/decade for VIIRS and MODIS, respectively. Over the entire globe (Figure 3c), the time series are very similar to those over nonpolar regions, with the differences averaging around -0.015 and CF trends for CV1S and CM4A at -0.6 and -0.9 %/decade. As indicated in Figure 2c, the differences are not uniform across the globe, but vary with latitude and surface type.
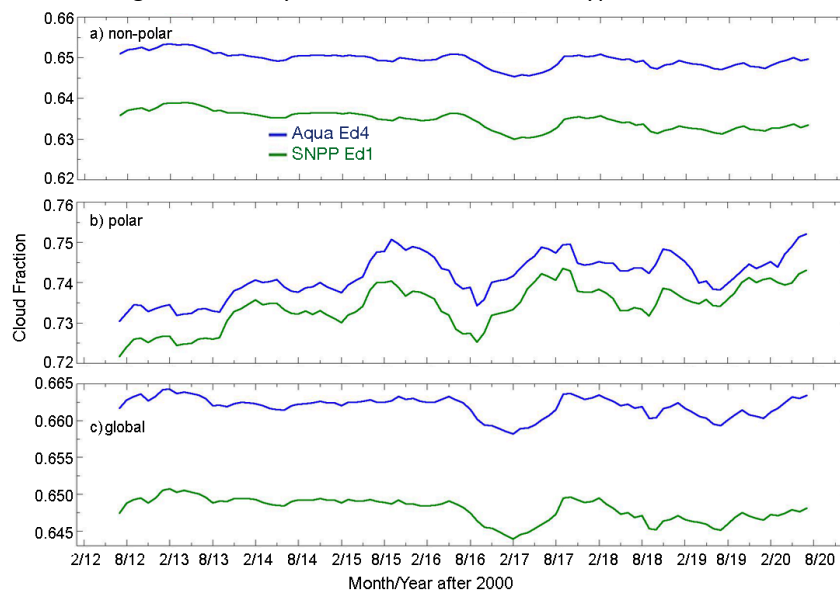

Figure 3. Time series of 12-month running mean daytime cloud amount over (a) nonpolar and (b) polar areas, and the (c) globe for Aqua Ed4 (blue) and SNPP Ed1a (green).
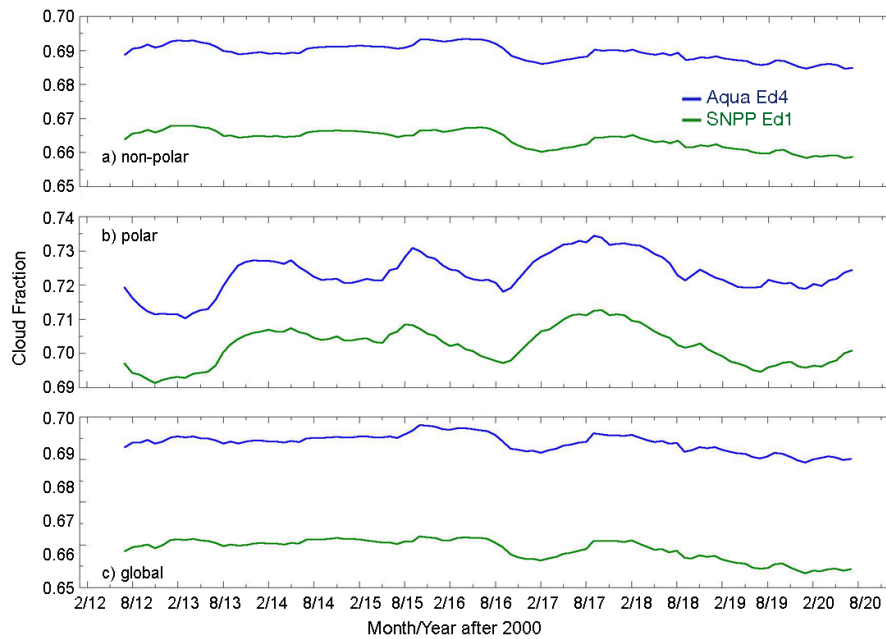
5

Figure 4. Same as Figure 3, except for nighttime.

At night (Figure 4), the differences appear fairly constant with time at all latitudes. Over the nonpolar regions (Figure 4a), CF(V) is 0.025 less than CF(M), while the V1S and CM4A trends of -0.9 and -0.7 %/decade reflect a slight divergence with time. The difference over the polar areas (Figure 4b) begins around 0.18 and ends around 0.25, resulting in a mean difference of 0.022. The trend in the differences is most likely due to the use of the revised thermal channel calibrations employed for Aqua MODIS after 2015, which resulted in more cloud detection. Because of the CM4A calibration, the CF(M) polar trends are unreliable. Nocturnal cloud detection was unaffected by the 2016 change in VIIRS data because only solar channels were altered. For this period, CF trends are evident day and night with decreasing (rising) cloudiness in the nonpolar (polar) regions. A decrease is evident when the whole Earth is considered.

Table 3 summarizes the mean cloud fractions from Aqua and VIIRS for the period, 2012-2020. During the daytime, the VIIRS averages are 0.016 less than Aqua over all marine areas and 0.014 less over land regions. Overall, the means differ by -0.015 during the day. At night, the discrepancies are more substantial, with differences of around –0.040 over oceans. Over land, the nocturnal differences are positive over nonpolar regions and are essentially zero over polar regimes. For all surfaces over the globe, the nighttime 9-year difference, CF(V) – CF(M), is -0.026.

Since the VIIRS pixel footprint changes little with VZA compared to that of MODIS, it is important to determine the differences, if any, in the properties as a function of VZA. Figure 5 plots the average global cloud fractions from CM4A and CV1S for 2013. Mean CF increases with VZA for both retrievals during the day and night, but less so for CV1S than for CM4A. On average, CF rises by 11% from near nadir to VZA = 65° for CV1S compared to 14% for CM4A. Thus, the nearly constant pixel size appears to have reduced the tendency for increasing cloudiness, perhaps by offering views of more clear areas between clouds. However, the increasing cloudiness with VZA cannot be eliminated by simply changing the pixel size, because the vertical extent of clouds can block the observation of breaks between clouds when viewed off nadir (e.g. Minnis 1989).

Table 3. Fractional mean cloud amounts from Aqua Ed4 and SNPP Ed1a for 2012-2020.

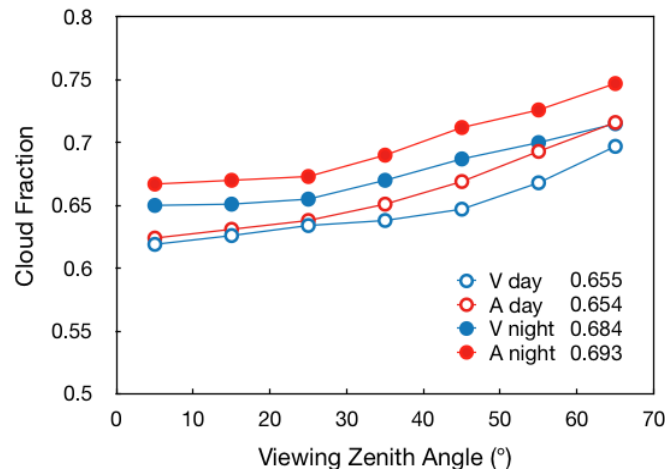|	**Ocean**			**Land**			**Ocean & Land**		
	Non-polar	Polar	Global	Non-polar	Polar	Global	Non-polar	Polar	Global
Day									
Aqua (Ed4)	0.690	0.847	0.703	0.535	0.627	0.551	0.649	0.748	0.660
SNPP (Ed1a)	0.674	0.836	0.687	0.521	0.621	0.538	0.634	0.740	0.645
Night									
Aqua (Ed4)	0.745	0.846	0.755	0.531	0.583	0.542	0.689	0.727	0.694
SNPP (Ed1a)	0.703	0.807	0.714	0.549	0.582	0.556	0.663	0.705	0.668

Figure 5. Mean 2013 global cloud fraction as a function of viewing zenith angle for Aqua CM4 (A) and CVS1 (V).

This VZA dependence affects the averaging of the cloud properties. In the previous reports on the CERES MODIS cloud properties (see Minnis et al. 2008, Minnis et al. 2011, Trepte et al. 2019, and Minnis et al. 2021), the monthly averages were computed by summing up the number of cloudy pixels falling in the region and dividing by the total number of pixels in the region. Annual and multiannual averages were then computed from these monthly means. The results for CERES MODIS Ed2 and Ed4 were averaged in that manner. But that approach is faulty if the footprint size increases with rising VZA and there is a relationship between the parameter of interest and VZA, e.g., Figure 5. For MODIS, the footprint size enlarges with increasing VZA according to the sec(VZA). Thus, for a fixed area, fewer pixels that are assigned to that region as VZA increases. As a result, overpasses viewing the area at a large VZA contribute fewer pixels to the monthly mean than their low VZA counterparts. This is not an issue if there is no dependence of the target variable on VZA. Yet most cloud properties vary systematically with VZA.

A true monthly average would ideally give equal weight to each day of the month when a region was viewed by the imager. With the approach above, days with high-VZA sampling have less influence on the mean than other days. To remedy this potential problem, daily averages are first computed for each region. The monthly means are then computed from the daily averages. This revised method is employed here for both datasets. The curves in Figure 5 suggest that the original approach will tend to underestimate the monthly means. That is indeed the case for CM4A, as the means reported by Trepte et al. (2019) are 0.010 less than those in Table 3, assuming the differences in averaging periods have negligible impact on the long-term averages. There is a small decrease in CV1S revised method here because the pixel size effectively remains constant. This revised method is employed for all VIIRS and CM4 products discussed here, and it will be applied to all future averages reported for the CERES MODIS and VIIRS cloud datsets.

From these comparisons, it is clear that the CV1S cloud fractions are mostly consistent with their Aqua counterparts, but are smaller during the daytime and more so at night. The differences have some surface type and regional variations. Further alterations of the CERES cloud mask to more closely align the results from VIIRS and MODIS need to account for those regional discrepancies.

Cloud phase
Because of dissimilarities in the available channels and the total cloud fractions, some disagreement is likely between the CV1S and CM4 cloud phase selections. The 2013 mean CV1S liquid cloud amount CFw and differences with CM4A in Figure 6 illustrate those

7

discrepancies. CFw from CV1S (Figure 6a) is greatest over the marine areas under the subtropical highs, the midlatitudes, and the Arctic. It is least over desert areas including Antarctica. The daytime liquid cloud amount differences, CV1S-CM4A, in Figure 6b reveal that generally CV1S classifies fewer tropical pixels as water clouds compared to CM4A. Over the midlatitudes and polar regions, the differences flip so that more clouds are classified as liquid by CV1S than by CM4A. As listed in the table in Figure 6, the mean difference in liquid cloud cover during the day is -0.005 for the globe as a whole, but is 0.034 over polar areas. The CV1S polar ice cloud amounts CFi are 0.052 less than their CM4A counterparts, while the global mean CFi is 0.014 less than the CM4 average. At night (Figure 6c), the CV1S liquid cloud amounts are less than the CM4A means over most oceanic areas, with the greatest absolute differences in the trade cumulus areas. The CV1S liquid clouds exceed the Aqua values over mountainous and arid regions. In polar areas, the differences in liquid cloud amount are -0.015 compared to -0.009 over the entire Earth. The VIIRS ice cloud amounts (table in Figure 6) are less than their Aqua counterparts. These lower amounts for each phase reflect the overall smaller CV1S nocturnal cloud amount. The global liquid fraction relative to the total amount is the same for both datasets: 62% and 53% for day and night, respectively.

a) SNPP VIIRS Ed1, water, day   b) SNPP VIIRS Ed1a, water, night

	Day	
Total	NPP	Aqua
Ice	0.238	0.252
Water	0.404	0.409
Polar		
Ice	0.251	0.303
Water	0.452	0.418
	Night	
Total	NPP	Aqua
Ice	0.316	0.329
Water	0.354	0.363
Polar		
Ice	0.417	0.427
Water	0.279	0.294

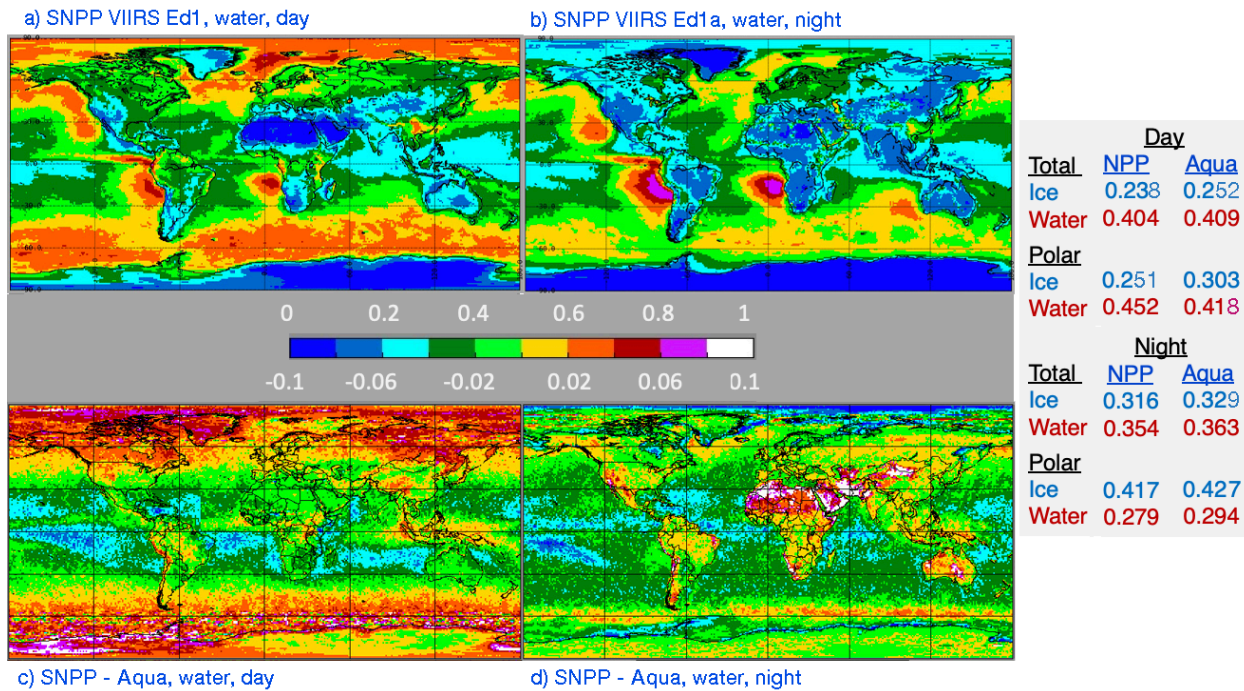c) SNPP - Aqua, water, day   d) SNPP - Aqua, water, night

Figure 6. Mean 2013 liquid cloud amounts from CV1S for (a) day and differences between CV1S and CM4A for (b) day and (c) night. The table lists the average liquid and ice cloud amounts for the globe and polar regions only.

The time series in Figure 7 reveal that at the beginning of the SNPP period, CV1S liquid cloud fractions are ~0.008 less than those from Aqua during the daytime (Figure 7a), but converge to within 0.002 of the CM4A amounts in 2016 and thereafter. At night (Figure 7b), the liquid cloud fraction from CV1S rises from ~0.351 in 2012 to ~0.356 in 2014, before slowly decreasing down to ~0.352 in 2018. The CM4A liquid fraction ~0.016 greater than its SNPP counterpart, then converges with CV1S and decreases after 2014. This is due to problems with the Aqua MODIS channels 27 and 29 in the Collection 5 dataset. Those channels are employed in the nocturnal phase selection algorithm. The MODIS Collection 6.1 data were used for CM4 starting in 2016, so the CM4A averages rose some after 2015 and the difference between CV1S and CM4A is relatively constant thereafter at ~0.010. Thus, the variation in the nighttime phase differences is due mainly to problems with MODIS than with CV1S. The daytime phase selection also uses the troublesome channel-29 data, but much less frequently than at night, so there is minimal impact during the day. The ice fraction variations (not shown) complement the results in Figure 7.
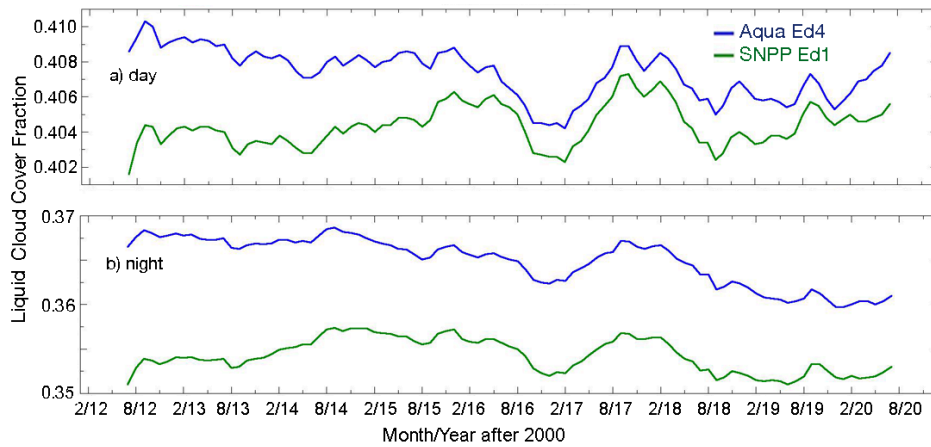
Figure 7. Global 12-month running mean liquid water fraction of total cloud amount from CM4A (blue) and CV1S.

Table 4. Same as Table 3, except for water cloud fraction.

	Ocean			Land			Ocean & Land		
	Non-polar	Polar	Global	Non-polar	Polar	Global	Non-polar	Polar	Global
Day									
Aqua (Ed4)	0.441	0.563	0.450	0.305	0.298	0.302	0.405	0.443	0.408
SNPP (Ed1a)	0.429	0.595	0.442	0.304	0.323	0.306	0.396	0.475	0.403
Night									
Aqua (Ed4)	0.436	0.414	0.434	0.207	0.158	0.197	0.375	0.299	0.366
SNPP (Ed1a)	0.414	0.400	0.412	0.228	0.152	0.212	0.365	0.289	0.355

The liquid phase fraction averages for the whole period are summarized in Table 4. In general, the results in Figure 6 are quite representative of the 9-year means. Over nonpolar ocean, the CV1S mean CFw is 0.012 less than its CM4A counterpart, while over polar ocean, the CV1S liquid fraction is 14% greater than CFw from CM4A during daytime. At night, when the VIIRS total cloud fraction is reduced relative to CM4A, the nonpolar ocean difference is -0.026. Globally, the mean land CFw for CV1S is 0.004 and 0.015 greater than CFw from CM4A, respectively, for day and night. At night, the corresponding differences are 3.7% and -0.4%. For all surfaces, globally, the respective day and night differences in liquid cloud fraction are -1.1% and -3.0%, on average.

Standard cloud height, pressure, and temperature

In this section all parameters are related because the cloud effective temperature T_c is used to ascertain cloud effective height Z_c and the height, in turn, is used to select the pressure. Effective cloud height derived from VIIRS should be an altitude somewhere between the top and base of the cloud. It corresponds to the mean radiating temperature of the cloud. For water clouds, the level of T_c is usually within a few meters to 100 m of the top. For cirrus clouds, it can be close to the cloud base or near cloud top depending on the density and physical thickness of the cloud. For water clouds, the true cloud top height Z_t is based on a small adjustment to the effective height, while for optically thin ice clouds, it is determined as a function of T_c and τ or cloud emissivity (Minnis et al. 2011a). For CM4, a new parameterization based on Minnis et al. (2008c) was implemented for opaque ice clouds. However, a coding error overwrote the results of the new parameterization in the final version of CM4 and it needs to be applied by the user (Minnis et al., 2021). That issue was corrected for CV1S. Cloud base height Z_b is estimated as the difference between Z_t and cloud thickness, ΔZ, which is estimated from T_c, τ, and cloud phase using various empirical formulae as described by Minnis et al. (2021). Cloud base temperature and pressure are found from the soundings based on Z_b. The results here focus primarily on cloud effective height since it is consistently determined from both CM4 and CV1S, and discussion of pressure would be somewhat redundant.
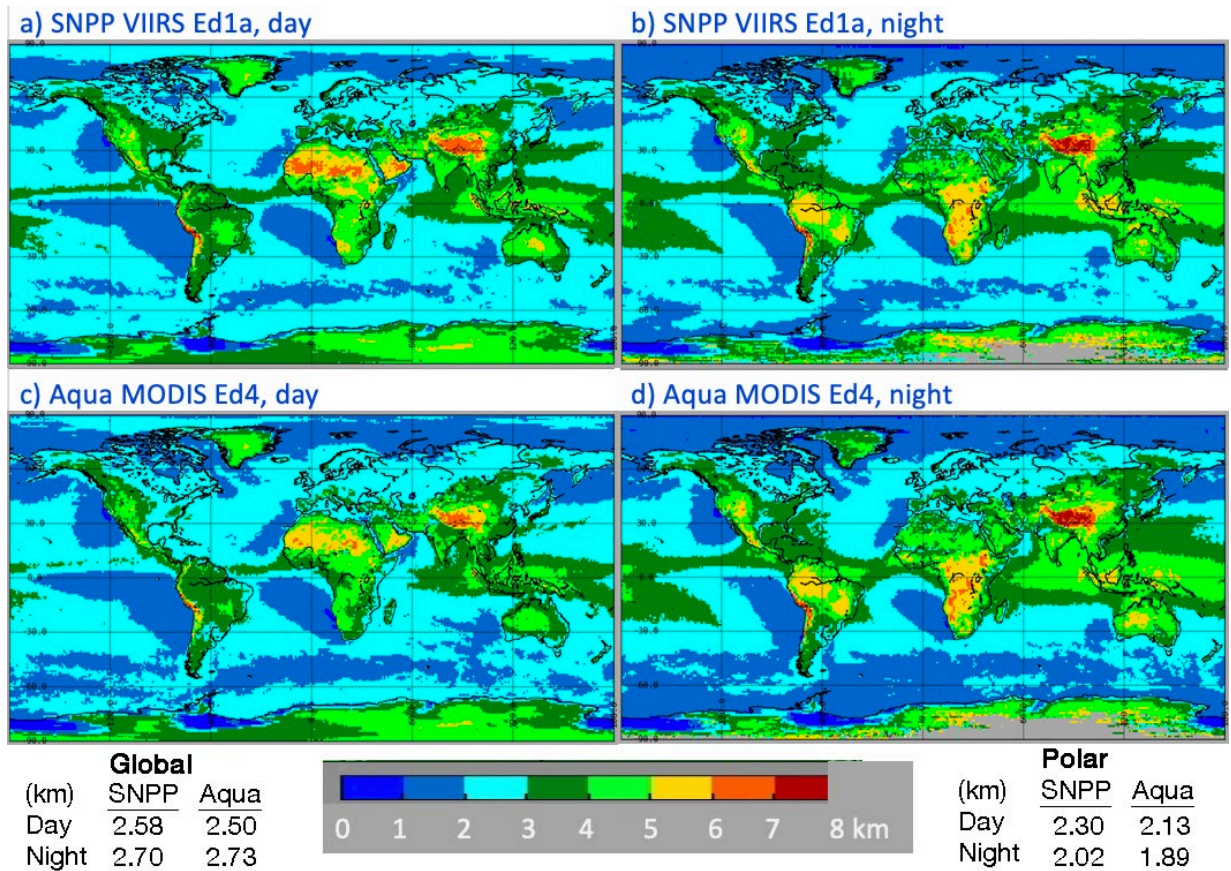
9

a) SNPP VIIRS Ed1a, day

b) SNPP VIIRS Ed1a, night

c) Aqua MODIS Ed4, day

d) Aqua MODIS Ed4, night

Global (km)	SNPP	Aqua
Day	2.58	2.50
Night	2.70	2.73

0 1 2 3 4 5 6 7 8 km

Polar (km)	SNPP	Aqua
Day	2.30	2.13
Night	2.02	1.89

Figure 8. Mean 2013 daytime water cloud effective heights from S-NPP Ed1a during (a) day and (b) night and from CM4A for (c) day and (d) night.
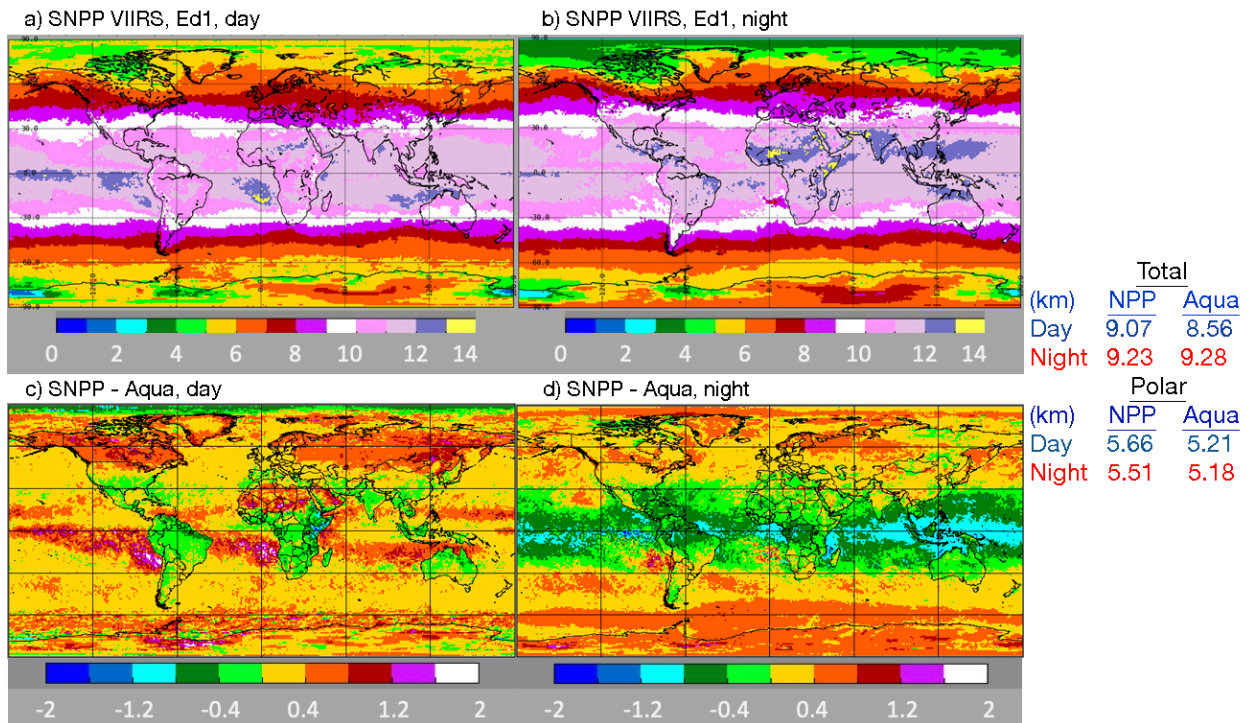
a) SNPP VIIRS, Ed1, day

b) SNPP VIIRS, Ed1, night

0 2 4 6 8 10 12 14

Total (km)	NPP	Aqua
Day	9.07	8.56
Night	9.23	9.28

c) SNPP - Aqua, day

d) SNPP - Aqua, night

Polar (km)	NPP	Aqua
Day	5.66	5.21
Night	5.51	5.18

-2   -1.2   -0.4   0.4   1.2   2   -2   -1.2   -0.4   0.4   1.2   2

Figure 9. Mean 2013 ice cloud effective heights from CV1S during (a) and (b), and the CV1S minus CM4a differences for (c)day and (d) night.

10

Figure 8 maps the 2013 mean water cloud effective heights for both CM4A and CV1S. During the day, CV1S (Figure 8a) yields patterns in Z_c that are quite similar to those for CM4A (Figure 8b), although the former heights are generally greater than the latter values, on average, by 0.08 km. The most notable discrepancies are seen over many land areas and over the equatorial convergence zones. The nocturnal distributions are similar, but again, Z_c from CV1S (Figure 8b) exceeds that from CM4A (Figure 8d) by 0.17 km. The most obvious differences are found over the Southern Ocean. For ice clouds (Figure 9), daytime Z_c(V) varies zonally for the most part (Figure 9a) much like Z_c(A) (not shown). Z_c(V) exceeds Z_c(A) over all areas except over tropical land (Figure 9c). At night (Figure 9b), Z_c(V) is significantly less than Z_c(A) over all tropical surfaces, but is greater than Z_c(A) for most regions poleward of 30° latitude. On average for 2013, Z_c(V) is 0.51 km greater than Z_c(A) over all areas during the day, while the two mean heights differ by only -0.05 km at night.
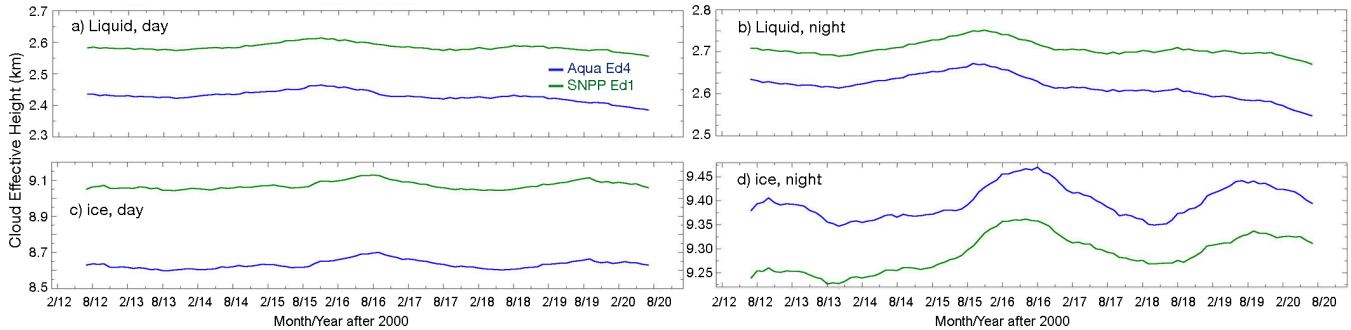

Figure 10. Same as Figure 7, except for mean liquid (top) and ice (bottom) cloud effective height for day (left) and night (right).

Table 5. Same as Table 3, except for mean cloud effective height (km).

	Day								
	Ocean			**Land**			**Ocean & Land**		
	Non-polar	Polar	Global	Non-polar	Polar	Global	Non-polar	Polar	Global
Water									
Aqua (Ed4)	2.23	1.99	2.20	3.48	2.42	3.32	2.48	2.13	2.44
SNPP (Ed1a)	2.35	2.14	2.33	3.75	2.63	3.56	2.63	2.30	2.59
Ice									
Aqua (Ed4)	9.33	5.45	8.98	9.22	5.45	8.39	9.29	5.44	8.79
SNPP (Ed1a)	9.71	5.83	9.41	9.41	5.92	8.71	9.63	5.88	9.20
	Night								
	Ocean			**Land**			**Ocean & Land**		
	Non-polar	Polar	Global	Non-polar	Polar	Global	Non-polar	Polar	Global
Water									
Aqua (Ed4)	2.51	1.74	2.43	3.86	2.22	3.60	2.70	1.89	2.62
SNPP (Ed1a)	2.57	1.95	2.51	3.85	2.37	3.65	2.78	2.09	2.71
Ice									
Aqua (Ed4)	10.19	5.13	9.50	10.57	5.44	9.27	10.29	5.26	9.43
SNPP (Ed1a)	9.93	5.57	9.35	10.47	5.82	9.28	10.08	5.68	9.32

The time series of cloud heights are given in 12-month running global means in Figure 10. Daytime liquid cloud heights (Figure 10a) from SNPP closely track those from Aqua with an offset of ~0.15 km. Both have a slight downward trend. Similar behavior is seen at night (Figure 10b) with a starting difference of ~0.11 km ending at ~0.13 km. The downward trend is also quite evident. During the day, the average ice cloud heights from CV1S follow their CM4A counterparts very closely with an offset of ~0.50 km. Both curves exhibit a slight upward trend. This trend is more apparent at night, when the two averages increase over the period and differ from ~-0.07 km to -0.01 km over the period. The variable ice cloud differences probably arise from the change in phase fractions at night due to the Aqua channel issues mentioned above.

Table 5 summarizes the means for the 9-y period. The cloud height differences are greater over land than over water during the day for liquid clouds and vice versa during the night. Differences over the polar regions are nearly identical to those over other areas during the day and somewhat larger at night. The CM4A ice clouds are higher, on average, than their CV1S counterparts during the night and vice versa during the day in line with the plots in Figure 10. Globally, CV1S ice cloud heights are 0.41 km higher than those from CM4A during the day, but 0.11 km lower than their Aqua counterparts at night. The sources for these differences are objects for further investigation.
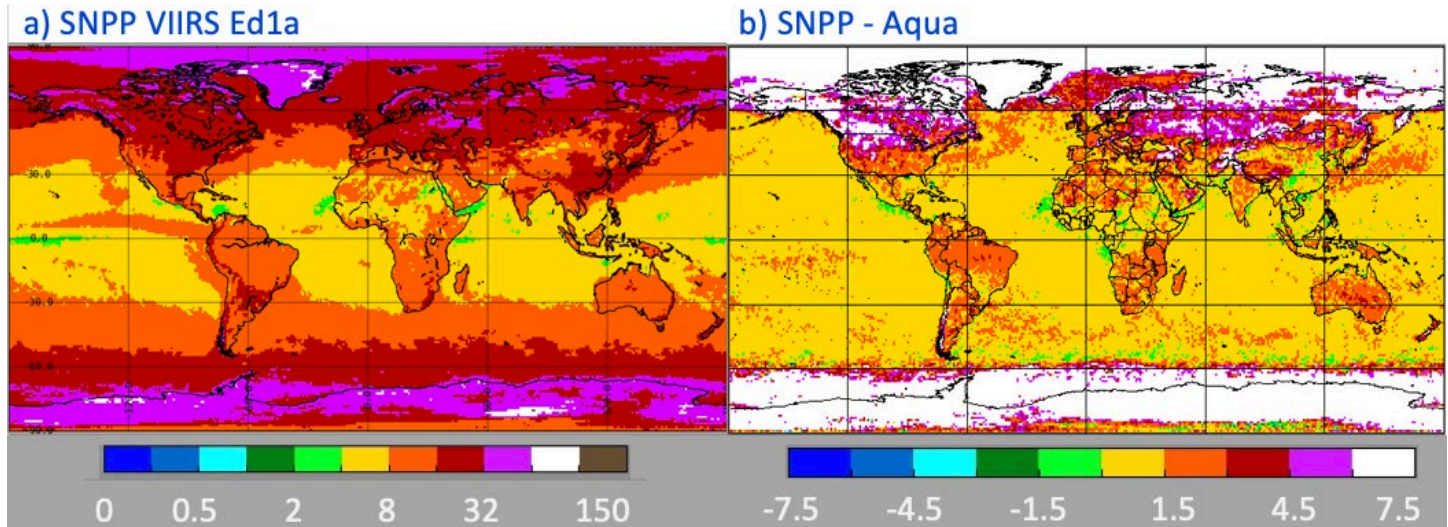
Figure 11. Mean 2013 daytime water cloud (a) SNPP optical depth and (b) difference in optical depth, $\tau(V) - \tau(M)$.

Standard daytime cloud optical depth, effective particle size based on 3.74-μm channel

The global distribution of SNPP Ed1a daytime mean water and ice cloud optical depths are shown in Figure 11 and Figure 12, respectively, along with their differences relative to the Aqua Ed4 means. Average CV1S liquid water τ is greatest in the midlatitudes and polar regions (Figure 11a), while for ice clouds (Figure 12a) it peaks in the areas of tropical deep convection and in the midlatitude storm tracks. For liquid clouds, $\tau(V)$ exceeds $\tau(M)$ by 6 or more over much of the polar snow and ice areas (Figure 11b), but differs from $\tau(M)$ by less than 1.5 over most of the nonpolar oceans. Over many land areas, $\tau(V)$ exceeds the CM4A mean. For ice clouds, $\tau(V)$ < $\tau(M)$ over most areas. Positive differences are seen over the Southern Ocean and near the Russian-Mongolian border (Figure 12b). The larger liquid water values from SNPP are mainly due to the calibration of 1.24-μm channel on VIIRS. The VIIRS Ed1a 1.24-μm reflectances are ~4% greater than their Aqua counterparts resulting in significantly larger τ values, compared to CM4A, particularly for larger optical depth clouds. Smaller ice cloud $\tau(V)$ values are due to replacement of the reflectance LUT used in the 1.24-μm CM4A retrievals, calibration differences, and slight discrepancies in the clouds selected as ice (e.g., Table 4).
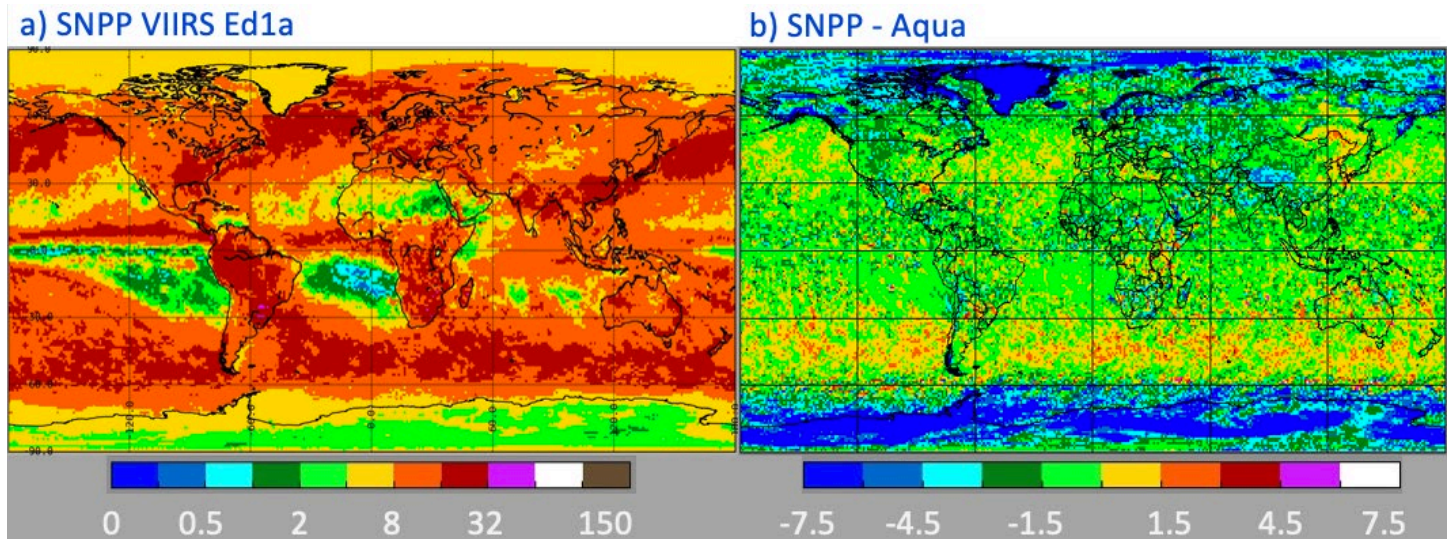
Figure 12. Same as Figure 11, except for daytime ice cloud optical depth.

The calibration effect is more evident in the time series of global running mean optical depth in Figure 13. Mean $\tau(V)$ for liquid water clouds (Figure 13a) is ~1.8 greater than $\tau(M)$ before 2016, when $\tau(V)$ rises by roughly 0.5. The rise is more pronounced for ice clouds (Figure 13b); $\tau(V)$ increases by more than 1.0 in 2016, surpassing the average $\tau(M)$ before returning to equivalency in late 2018. Both ice and water $\tau(V)$ drop slightly after 2017. Further examination revealed that the increases after 2016 occur mainly in the nonpolar regions, as expected since τ is retrieved using the visible channel reflectance over snow/ice-free surfaces.
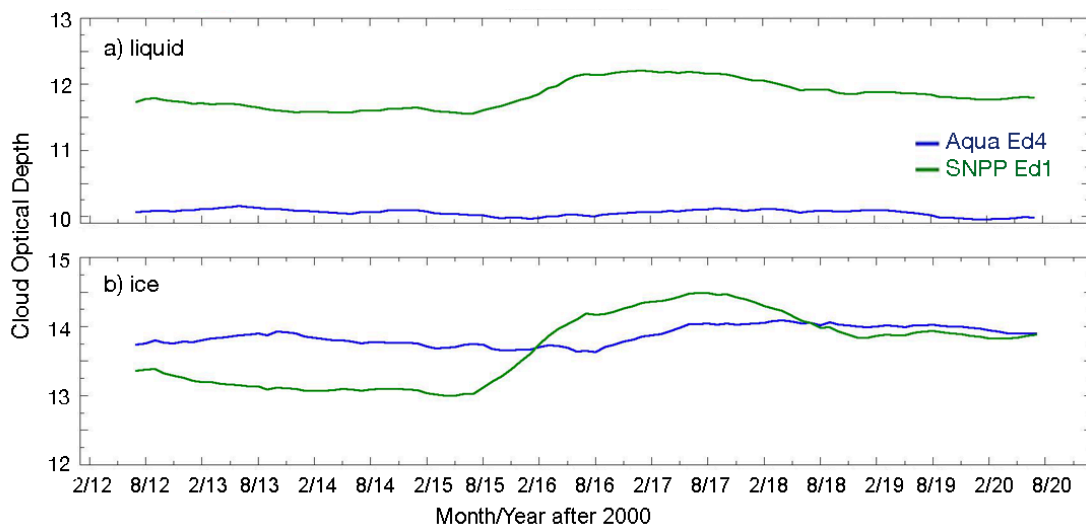

Figure 13. Non-polar 12-month running mean daytime cloud optical depth from CM4A and CV1S for (a) water and (b) ice clouds.

Table 6. Same as Table 3, except for daytime mean cloud optical depths.

	Ocean			Land			Ocean & Land		
	Non-polar	Polar	Global	Non-polar	Polar	Global	Non-polar	Polar	Global
Water Clouds									
Aqua (Ed4)	9.15	18.65	10.12	13.75	23.82	15.28	10.04	19.98	11.17
SNPP (Ed1a)	10.57	26.55	12.35	16.81	34.16	19.75	11.82	28.64	13.91
Ice Clouds									
Aqua (Ed4)	13.48	13.73	13.54	15.20	12.82	14.71	13.88	13.43	13.85
SNPP (Ed1a)	13.50	11.05	13.31	14.44	7.65	12.93	13.71	9.33	13.18

The mean differences between the two datasets can be quantified from the average optical depths given in Table 6 for the period, 2012-2020. Over non-polar ocean and land, the liquid cloud τ(V) averages are 1.4 and 3.1 greater than τ(M). For all nonpolar regions, SNPP water τ is 1.8 or about 18% greater than the CM4A mean. This can be contrasted with the nonpolar ice τ(V), which is 0.2 less than its CM4A equivalent. The liquid and ice τ differences over the polar zones are 8.7 and -4.1. That is, the polar τ(V) means are 43% greater and 31% less than the liquid and ice cloud τ(M) values, respectively. These differences in optical depth over the poles are likely due to differences in phase selections over the polar regions (e.g., Table 4). The positive differences in nonpolar regions is probably the result of several factors including possible calibration discrepancies, slightly smaller VIIRS cloud fractions (perhaps fewer low-τ clouds detected), and the higher resolution VIIRS pixels, which would tend to yield greater optical depths in a linear average sense (e.g., Minnis et al. 2016).

Figure 14 plots the mean τ values for 2013 as a function of VZA for SNPP and Aqua. Optical depth from VIIRS tends to vary less with VZA than its Aqua counterparts. For liquid water clouds (Figure 14a), the τ(V) curve drops with increasing VZA until rising again for VZA > 55°. The change with VZA is only 7% between 0 and 70° for CV1S mean optical depths over all surfaces, compared to 22% for CM4A. For ice clouds (Figure 14b), however, the change in τ(V) is ~13% compared to 22% for τ(M). The smaller drop with VZA for VIIRS is likely due to VIIRS' smaller pixel size at the more oblique angles relative to that from Aqua MODIS, since optical depth tends to decrease with increasing pixel size (e.g., Table 15 of Minnis et al., 2016).

Regional averages of CV1S cloud droplet effective radius for 2013 are plotted in Figure 15 along with the differences between the VIIRS and Aqua means. Overall, the relative distribution of VIIRS R_e (Figure 15a) is quite similar to that for Ed4 (not shown, see Figure 15 from Minnis et al. [2021] for example). Yet, the magnitudes are clearly not the same as seen in Figure 15b. Negative differences of 1.0 µm or greater are common over nonpolar ocean areas, while positive differences are evident over Greenland, Alaska, Siberia, north Africa, and Antarctica. Ice crystal effective radius means from CV1S are plotted in Figure 16 along with the R_e(V) – R_e(M) regional differences. Much like their droplet counterparts, the VIIRS ice R_e regional averages are distributed in patterns similar to the CM4A values with a mostly zonal decrease from the poles to the tropics (Figure 16a). Superimposed on that zonal pattern are deviations resulting from climatological circulation patterns such as the ITCZ and those induced by the positioning of landmasses. Again, the magnitudes vary with small differences over ice-free water and large negative differences over the Arctic Ocean and parts of Antarctica and surrounding ocean (Figure 16b). Over land equatorward of 45° latitude, R_e(V) exceeds R_e(M) by up to 6 µm. The largest differences occur where ice clouds are sparse.
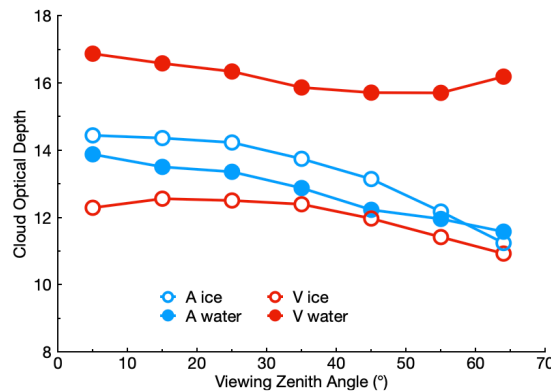

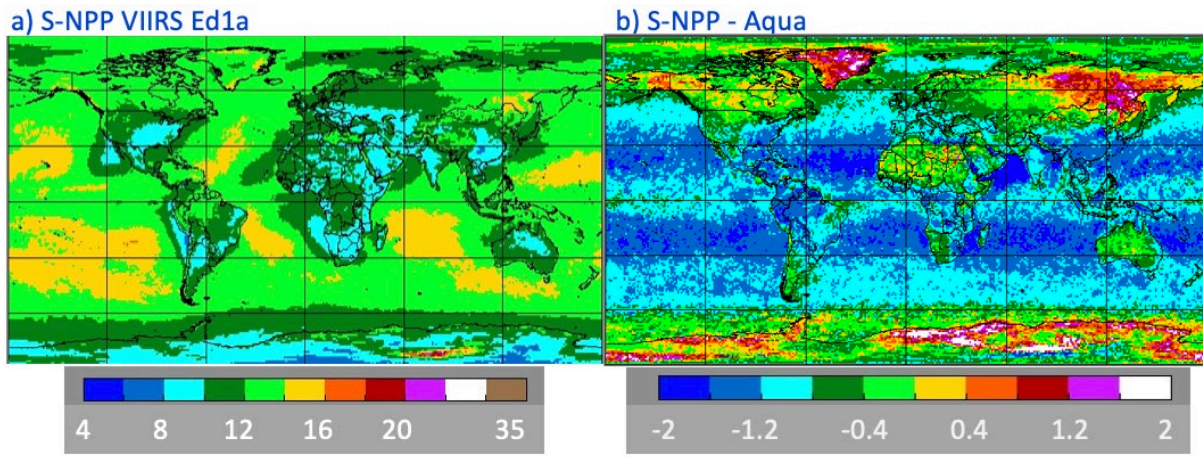Figure 14. . Same as Figure 5, except for (a) liquid and (b) ice cloud optical depth.

14

Figure 15. Same as Figure 11, except for daytime liquid cloud droplet effective radii.

The time series of global mean R_e in Figure 17 indicate that the differences between R_e(V) and R_e(M) are relatively constant throughout the 9 years for both water (Figure 17a) and ice (Figure 17b). For liquid clouds, the difference over polar regions is much smaller than that in Figure 17a. A slight upward trend, evident in R_e(V) and R_e(M) for water clouds, is primarily due to clouds over nonpolar areas (not shown).

Table 7 lists the mean r_e values from Aqua CM4A and CV1S for 2012-2020. Overall, liquid R_e(V) and ice R_e(V) are 1.0 and 0.8 µm less than those from Aqua, respectively. These global differences are mainly driven by retrievals over the nonpolar oceans where the mean VIIRS R_e(liq) and R_e(ice) are 1.2 µm and 0.8 µm, respectively, smaller than the CM4A averages. Larger deviations are found over the polar regions for R_e(ice) and over nonpolar land, the ice R_e(M) averages 0.7 µm less than the R_e(V). The differences between the VIIRS and Aqua retrievals of R_e can be due to a variety of factors. The main difference is the use of the new LUTs for VIIRS, which yield smaller values of R_e compared to the old LUTs, which employed the central wavelength of the SIR band to determine the optical properties. Another major source for the discrepancies is the inadvertent use of the smaller Aqua SIR solar constant, which tends to produce a greater reflectance and, hence, yields a lower value of R_e in the retrieval. Using the correct VIIRS SIR solar constant accounts for about a third of the difference. The remaining difference is likely due to the LUT changes.
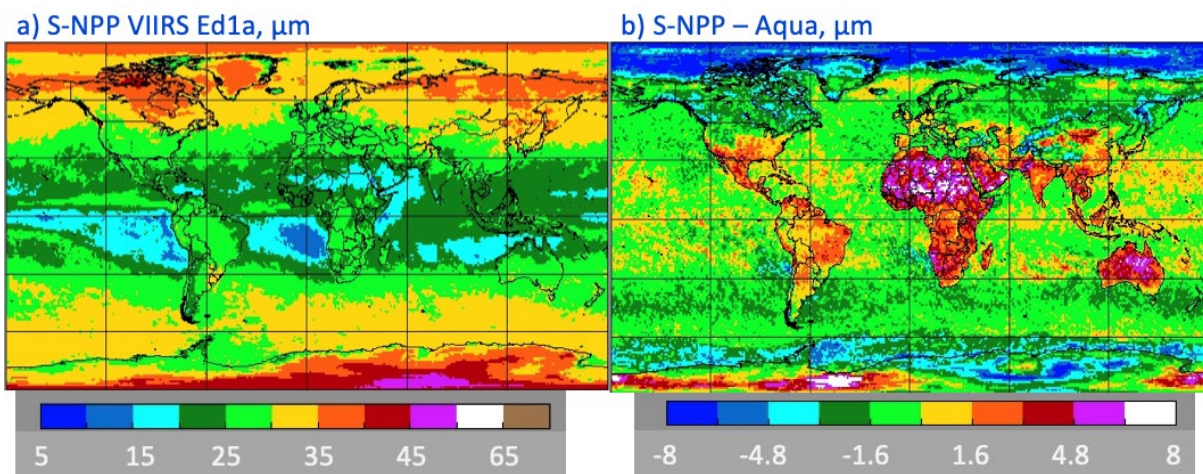

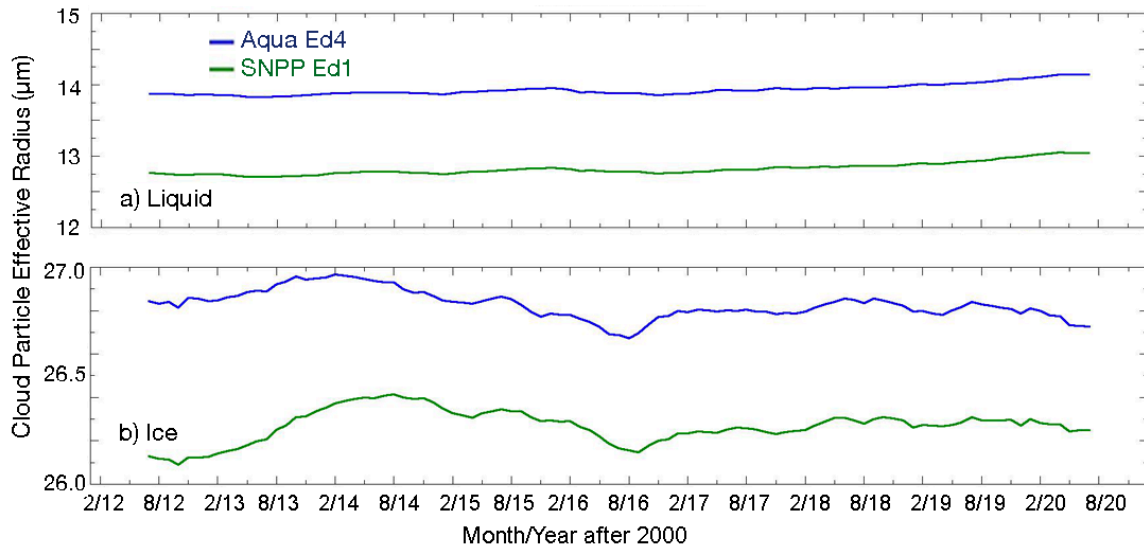Figure 16. Same as Figure 12, but for ice cloud.

Figure 17. Time series of 12-month running nonpolar mean standard (a) liquid and (b) ice cloud particle effective radius retrieved using the 3.74-µm channel using the CM4A and CV1S algorithms.

Mean R_e for all surfaces is plotted as a function of VZA in Figure 16 for the 2013 CV1S and CM4A retrievals. Unlike the optical depth variations, VIIRS R_e increases more with VZA than its MODIS counterpart. In this plot, R_e(liq) rises by ~12% for VIIRS compared to ~5% for CM4A. Likewise, R_e(ice) increases by 19% for CV1S, while it changes by +10% for CM4A. This larger change in R_e with VZA from the VIIRS retrievals is surprising given the smaller pixel size.

Table 8 shows mean liquid and ice water path from CM4A and CV1S for cloudy pixels only over the period 2012-2020. To obtain the total LWP or IWP, the results would need to be multiplied by the cloud fraction. Here, cloud water path CWP is computed as

$$CWP = 0.67\ R_e\ \tau, \tag{1}$$

under the assumption that the retrieved effective size is constant through the entire cloud vertical column. Alternatively, LWP can be estimated by multiplying the result of Eq(1) by 0.83 (Bennartz 2007) using the assumption that the retrieved R_e represents only the top layer of the cloud and the droplet size increases adiabatically with height in the cloud. The adiabatic assumption is more accurate in many areas (e.g., Dong and Minnis, 2022). Globally, the mean values differ by 30% for water clouds and -4% for ice clouds. The great difference for liquid water clouds is primarily due to the polar clouds, as LWP(V) is only 8% greater than LWP(M) in nonpolar areas. These differences track mostly with the optical depth differences since the R_e values are generally close. Globally, IWP(V) exceeds IWP(M) by only 4%.

The opposite dependencies of R_e and τ with VZA also tend to compensate each other when used to compute CWP. Figure 19 shows the mean 2013 IWP and LWP from CV1S and Aqua as functions of VZA. The curve for VIIRS LWP is relatively flat with minimal decrease up to VZA = 55°, but jumps by +11% in the last VZA bin. This bump at the end follows the less dramatic rises in both τ and R_e at the same point. Conversely, the mean CM4A LWP decreases almost monotonically from 0° to 64°, an overall drop of 11%. The CM4A IWP falls off more at the higher angles, resulting in a 17% drop relative to nadir. The VIIRS IWP curve is very flat, changing by only 4% with a maximum at 35°. Note, the means in Figure 19 may differ from those in Table 8 because of different geographical weighting in calculating the means.

Table 7. Same as Table 3, except for daytime mean cloud droplet radius and ice crystal effective radius (μm).

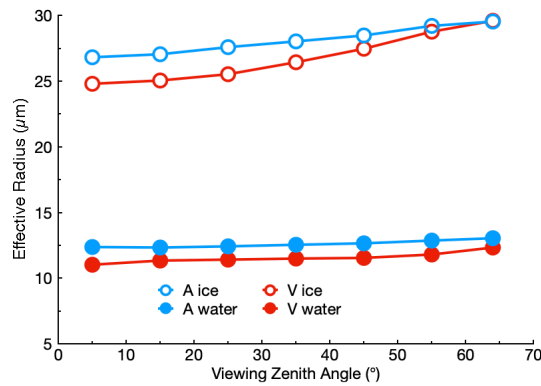|	Ocean			Land			Ocean & Land		
	Non-polar	Polar	Global	Non-polar	Polar	Global	Non-polar	Polar	Global
Water Cloud									
Aqua (Ed4)	14.51	12.46	14.31	11.63	11.94	11.70	13.94	12.30	13.77
SNPP (Ed1a))	13.32	12.03	13.19	10.90	12.22	11.15	12.83	12.07	12.75
Ice Cloud									
Aqua (Ed4)	26.75	33.98	27.41	26.87	35.08	28.76	26.82	34.51	27.83
SNPP (Ed1a)	25.86	31.69	26.29	27.53	33.82	28.85	26.27	32.75	27.00

Figure 18. Same as Figure 5, except for (a) liquid and (b) ice cloud particle effective radius.

Table 8. Same as Table 3, except for daytime mean liquid and ice cloud water-path (gm^{-2}) over cloudy areas only.

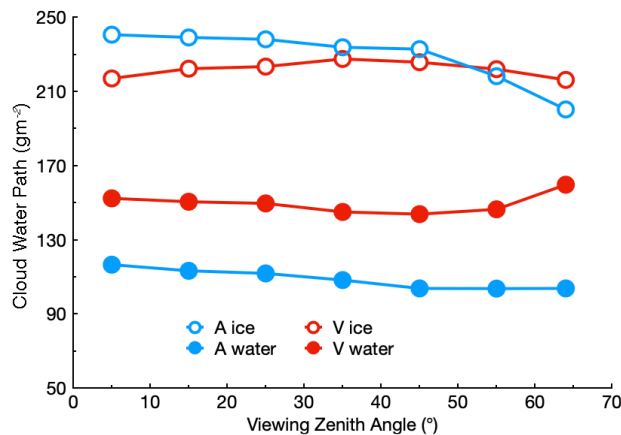|	Ocean			Land			Ocean & Land		
	Non-polar	Polar	Global	Non-polar	Polar	Global	Non-polar	Polar	Global
Water Cloud									
Aqua (Ed4)	86.6	165.6	94.8	107.3	234.0	126.4	95.6	182.6	101.1
SNPP (Ed1a)	94.0	291.3	116.1	139.4	434.2	189.2	103.1	329.7	131.4
Ice Cloud									
Aqua (Ed4)	237.2	239.3	238.1	259.2	250.4	258.5	242.1	247.2	243.5
SNPP (Ed1a)	262.9	199.2	257.8	274.4	146.7	245.4	265.1	172.0	253.7

Figure 19. Same as Figure 5, except for cloud water path.

Alternative products

The CERES project has a long-term perspective that includes adding new cloud properties to the SSF as they become available. These alternate products are currently not utilized in the operational determination of broadband fluxes in any of the CERES processing subsystems. However, they are included in the SSF for experimental purposes and further scientific analysis as they become more mature. Some have already been employed in various studies (e.g., Painemal et al., 2013, 2016). As they improve, some or all of these parameters may become part of the standard CERES processing, if they enhance the accuracy of the CERES flux products.

Cloud particle size retrievals

Figure 20 shows the global distribution of 2013 daytime liquid and ice cloud R_e means derived from reflectances at 1.24 μm (left) 1.62 μm (right). These may be compared with the standard retrievals in Figure 15a and Figure 16a based on 3.8 μm reflectances. The relative distributions of mean liquid water droplet radii at 1.24 μm (Figure 20a) and 1.60 μm (Figure 20b) are very similar, and, in turn, are not unlike those in Figure 15a, but the magnitudes are quite different. Except for the littoral areas under the subtropical highs or around Antarctica and in the Arctic Ocean, $R_e(1.24)$ tends to be less than $R_e(1.61)$. In nearly all cases, R_e from 3.74 μm is less than its alternative counterparts for liquid clouds.
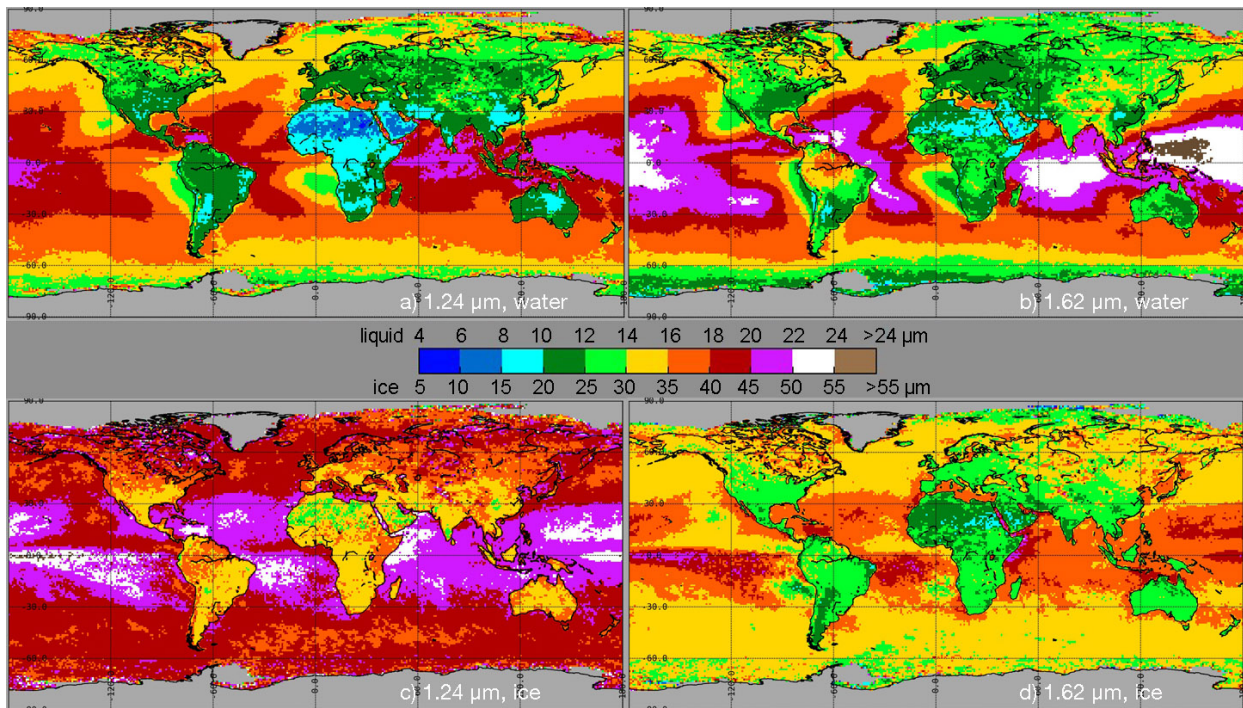

Figure 20.   SNPP VIIRS Ed1a mean R_e for liquid water clouds at (a) 1.24 μm and (b) 1.62 μm and for ice clouds at (c) 1.24 μm and (d) 1.62 μm, 2013.

For ice clouds, $R_e(1.24)$ in Figure 20c greatly exceeds $R_e(1.61)$ in Figure 20d. The latter is significantly larger than $R_e(3.74)$. While magnitudes are quite different, the patterns in Figure 20c and Figure 20d are similar. There are some discrepancies in the patterns between that in Figure 16a and those for $R_e(1.61)$ and $R_e(1.24)$. For example, the lower values of R_e increase westward from the coastal areas under the subtropical highs, while $R_e(3.74)$ remains relatively constant or even decreases to the west in some areas.

The time series of the alternative values (Figure 21) show discontinuities in 2016 for both liquid (Figure 21a) and ice cloud (Figure 21b) $R_e(1.24)$ averages for CV1S. The increase in the values after the beginning of 2016 may be attributed to the change in the 1.24-μm calibration. The $R_e(V)$ means are much closer to those from CM4A. Similarly, $R_e(1.61)$ from VIIRS for liquid clouds (Figure 21c) is much closer to $R_e(2.1)$ from Aqua after 2016. For ice clouds, $R_e(1.6)$ shows no increase after 2016 and parallels $R_e(2.1)$ through the whole period (not shown).

The 2013 R_e results, summarized in Table 9, reveal that, on average, CV1S liquid cloud $R_e(1.24)$ is 1.1 μm less than and 1.3 μm greater than $R_e(1.60)$over nonpolar and polar regions, respectively. This translates to a mean difference, $R_e(1.60) - R_e(1.24)$, of 0.8 μm over the

18

entire globe. The mean $R_e(1.60)$ and $R_e(1.24)$ exceed the global average $R_e(3.74)$ by 3.9 and 3.1 µm, respectively. On average, $R_e(1.61)$ is slightly less than that from $R_e(2.13)$ from CM4A, but is distributed in a similar pattern (not shown). However, the CV1S global mean $R_e(1.24)$ is identical to the CM4A mean, but the patterns are dissimilar (not shown), one of the reasons that the CM4A retrievals were not recommended for scientific use.

Overall for ice clouds, $R_e(3.74)$ is 6.0 µm smaller than $R_e(1.61)$, while $R_e(1.24)$ exceeds $R_e(3.74)$ by 14.9 µm. The CV1S $R_e(1.24)$ mean is 8% smaller than its CM4A counterpart, most likely because of the LUT problem in the 1.24-µm retrievals noted for CM4 (Minnis et al., 2021). The mean ice $R_e(2.13)$ from CM4A is 5.6 µm larger than that from the CV1S 1.6-µm retrieval. Given the results in Figure 21, it is expected that the Aqua and VIIRS long-term averages will be closer than those in Table 9, except R_e(ice) from 1.61 and 2.13 µm.

Discrepancies in the patterns and, perhaps, the magnitudes of the three distinct VIIRS R_e averages may be due in part to differences in the cloudy pixels that returned valid particle sizes for each wavelength. For example, over ocean, mean $R_e(1.24)$ for liquid water clouds is based on 64% of pixels having a $R_e(3.74)$ retrieval. For ice clouds, that fraction reduces to 53%. Likewise, at 1.61 µm those amounts are 59% and 77%, respectively. Some of differences in magnitude and pattern could be due to the alternative retrievals being successful for only a certain portion of the total sample.

To explore that idea further, histograms of R_e were generated from retrievals in all three channels. Examples of those histograms are provided in Figure 22 and Figure 23 for liquid and ice clouds, respectively. For the small optical depths, Re(3.74) in Figure 22e has an almost log- normal distribution for both land and water scenes, while $R_e(1.24)$ and $R_e(1.60)$ in Figure 22a and Figure 22c,
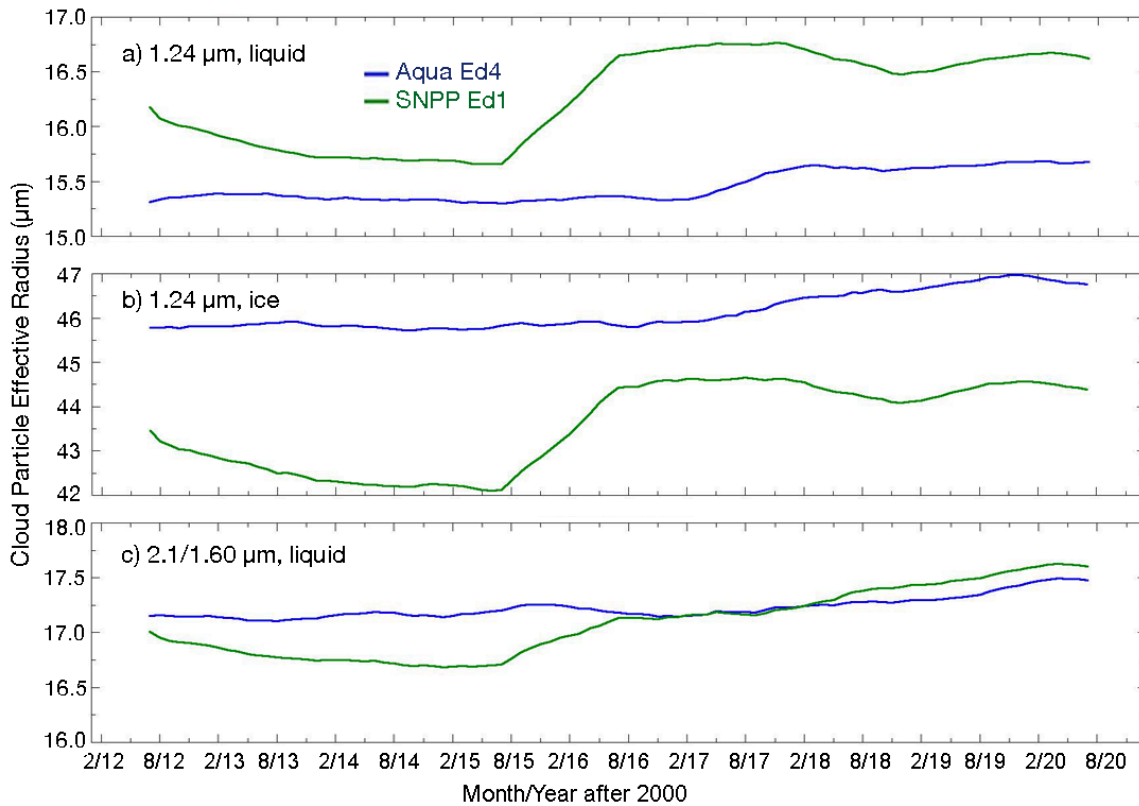

Figure 21. Same as Figure 17, except for R_e retrieved using 1.24-µm channel for (a) liquid and (b) ice clouds and (c) 2.1 or 1.6-µm for liquid clouds.

Table 9.   Daytime mean cloud droplet and ice crystal effective radius from 3.8, 1.6, 2.13, and 1.24 µm retrievals. Aqua Ed4 and SNPP Ed1a, 2013.

|	Ocean			Land			Ocean & Land		
	Non-polar	Polar	Global	Non-polar	Polar	Global	Non-polar	Polar	Global
Water Clouds									
Aqua (3.8)	14.4	12.4	14.1	11.6	12.1	11.7	13.8	12.3	13.6
SNPP (3.8)	13.2	12.1	13.0	10.7	12.3	11.0	12.6	12.1	12.5
Aqua (2.13)	18.0	13.8	17.5	13.6	13.8	13.7	17.1	13.8	16.7
SNPP (1.61)	18.0	13.2	17.5	12.6	13.4	12.7	16.8	13.2	16.4
Aqua (1.24)	15.9	17.4	16.0	13.6	15.5	13.8	15.4	17.0	15.6
SNPP (1.24)	17.1	14.7	16.9	10.9	13.8	11.3	15.7	14.5	15.6
Ice Clouds									
Aqua (3.8)	26.7	35.2	27.7	26.6	37.0	28.3	26.7	36.2	28.3
SNPP (3.8)	25.7	32.2	26.0	27.1	34.0	28.9	26.0	34.0	27.3
Aqua (2.13)	40.0	39.7	40.0	35.1	39.3	35.7	38.8	39.6	38.9
SNPP (1.61)	35.4	31.7	35.1	27.9	32.7	28.5	33.4	32.1	33.3
Aqua (1.24)	47.9	47.7	47.9	39.6	46.1	40.5	45.9	47.2	46.0
SNPP (1.24)	44.8	42.1	44.5	35.5	42.0	36.3	42.3	42.1	42.2
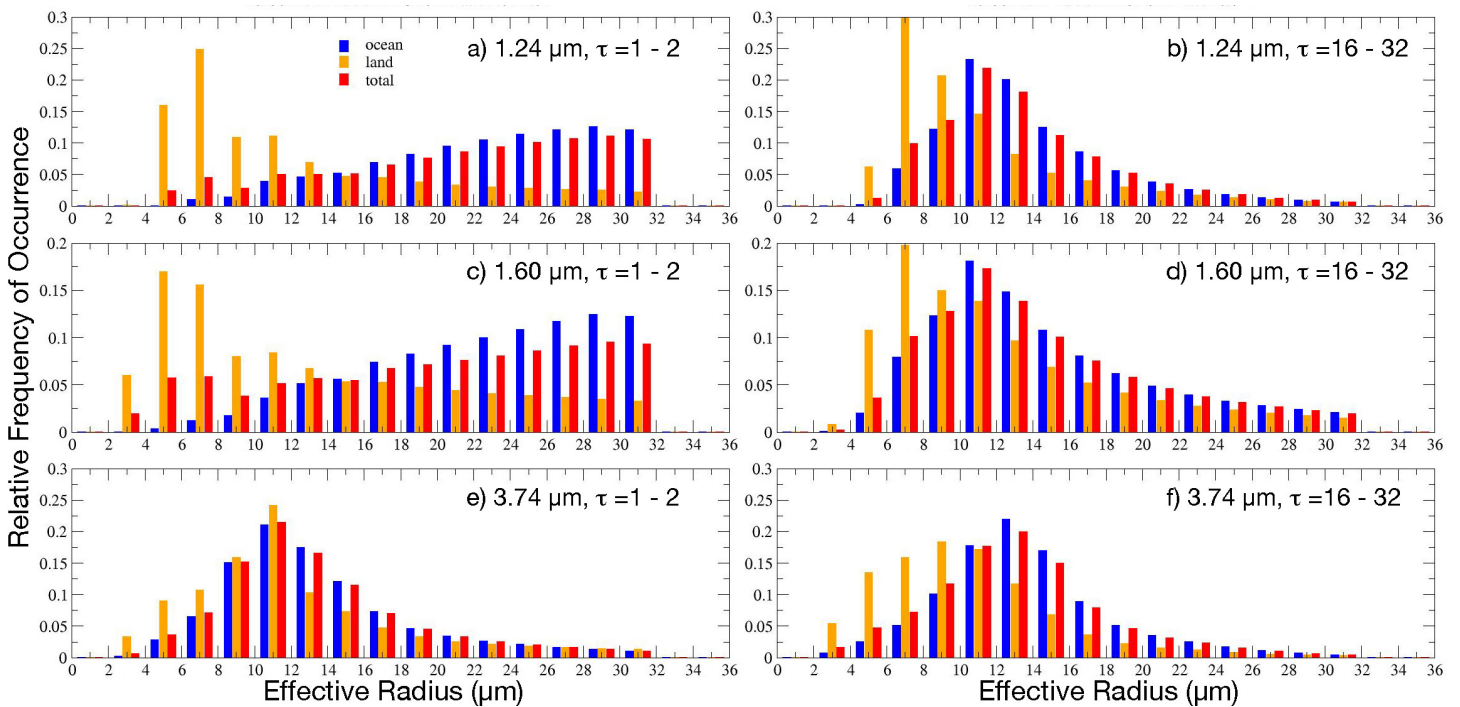
Figure 22.   Probability distributions of CSV1 liquid water droplet effective radii from (a, b) 1.24 µm, (c,d) 1.60 µm, and (e,f) 3.74 µm for optical depth ranges, left: 1 – 2 and right: 16-32, April 2013.

respectively, are nearly linearly distributed with maxima at the high end, ~28 µm, respectively, over water, and with low-end maxima for land surfaces. In this optical depth range, the droplet R_e means over all surfaces at 1.24, 1.60, and 3.74 µm are 21.2, 19.5, and 13.4 µm, respectively. Only 16 and 12% of the pixels having a value at 3.74 µm also had a retrieval at 1.24 and 1.60 µm. These results contrast with those for $16 \leq \tau < 32$, for which all three channels produce a log-normal distribution and the means range from 13.1 µm at 3.74 µm to 14.3 µm at 1.6 µm. In this case, 93 and 87% of the R_e(3.74) pixels yield valid retrievals at 1.24 and 1.60 µm, respectively.
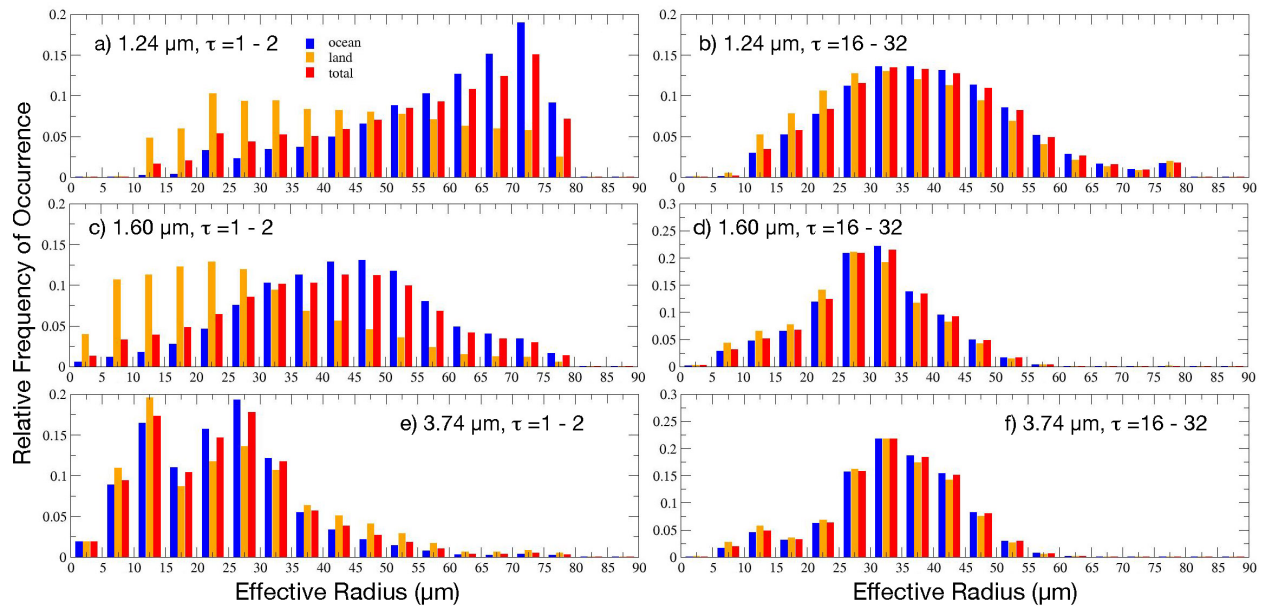
Figure 23. Same as Figure 20, except for ice clouds.

Probability distributions were created over the full range of optical depths and it was found that for τ between 4 and 8, the histograms became more like the log-normal distributions. Therefore, the data were averaged for $\tau < 6$ and for $\tau \geq 6$. The results were similar to those in Figure 22. For the lower range, the respective R_e means at 1.24, 1.60, and 3.74 µm are 18.8, 17.7, and 12.9 µm, compared to 13.8, 14.4, and 12.9 µm for the upper range. The fractions of the $R_e(3.74)$ retrievals represented by those numbers are 41 and 36.4% at 1.24 and 1.60 µm, respectively, for the lower τ's and 90 and 85% for the higher optical depths.

Similar results are found for ice clouds, although more reasonable values of R_e may found at lower optical depths at 1.60 µm than at 1.24 µm. Histograms of R_e for the same range of τ as in Figure 22, but for ice clouds, are presented in Figure 23. At low optical depths (Figure 23e), $R_e(3.74)$ has a mostly log-normal distribution except for the bump around 10 µm, which is due to the use of a default value of R_e needed to retrieve τ. The distribution for $R_e(1.24)$ in Figure 23a is comparable to that in Figure 22a, but has a greater slope. At 1.60 µm, however, a more log-normal type of distribution is found (Figure 23c). The means for $R_e(1.24)$ and $R_e(1.24)$ are 54 and 40 µm, respectively, compared to 24.4 µm at 3.74 µm with 11 and 84% of the $R_e(3.74)$ retrieval pixels having Re values at 1.24 and 1.60 µm. For the greater τ range, $R_e(3.74)$ averages 33.6 µm compared to 38.5 and 30.1 µm at 1.24 and 1.60 µm, respectively, based on corresponding sampling fractions of 95 and 99%. The distributions in Figure 23b, d, and f all appear to be more log-normal than those for the smaller optical depths. The findings for $\tau < 6$ and $\tau > 6$ are much like those for water clouds. The means for $R_e(1.24)$ are 47.5 and 36.7 µm, respectively, for the lower and higher τ range, compared to 22.5 and 32.8 µm at 3.75 µm. The corresponding $R_e(1.60)$ averages are 34.8 and 29.3 µm. The fraction retrieved at 1.60 µm rises from 61 to 97% at the upper end, compared to a rise from 41 to 89% at 1.24 µm.

These results suggest that the NIR retrievals at low optical depths are subject to significant uncertainties, a result found by Zhang and Platnick (2011) for stratiform water clouds. These uncertainties include errors in surface and aerosol reflectances, which are less important as the cloud becomes opaque. Also important is the behavior of reflectances at these wavelengths. Reflectances ρ at 1.24 µm (top) and 1.60 µm (bottom) taken from the CSV1 water droplet LUTs are plotted against the VIS reflectance in Figure 24 corresponding to a range of τ and R_e values at SZA = 45.6° and VZA = 31.8°. The plots in each row are for different relative azimuth angles (RAA) that increase from left to right. A relative azimuth angle of 0° is in the forward scatter direction, while 180° is backscatter. The reflectances ρ decrease at both wavelengths in a mostly monotonic fashion with R_e for a given value of τ, except at very low values of R_e. In Figure 24a, b, and c, the curve for $\rho(1.24)$ curve for $R_e = 2$ µm falls below those for larger radii over most of the τ range. Its drop increases as RAA rises. Coincidentally, separation of the curves for $R_e = 4$-8 µm also decreases with rising RAA increasing the uncertainty in the retrievals for smaller radii. The separation between the curves for $\rho(1.24)$ for all values of R_e is smaller than that for $\rho(1.60)$ suggesting that $R_e(1.60)$ should be less uncertain for a given retrieval. However, for both wavelengths, the curve separation is minimal for $\tau \leq 4$, indicating that the retrievals at those optical depths will be highly uncertain, a conclusion borne out by the observations.
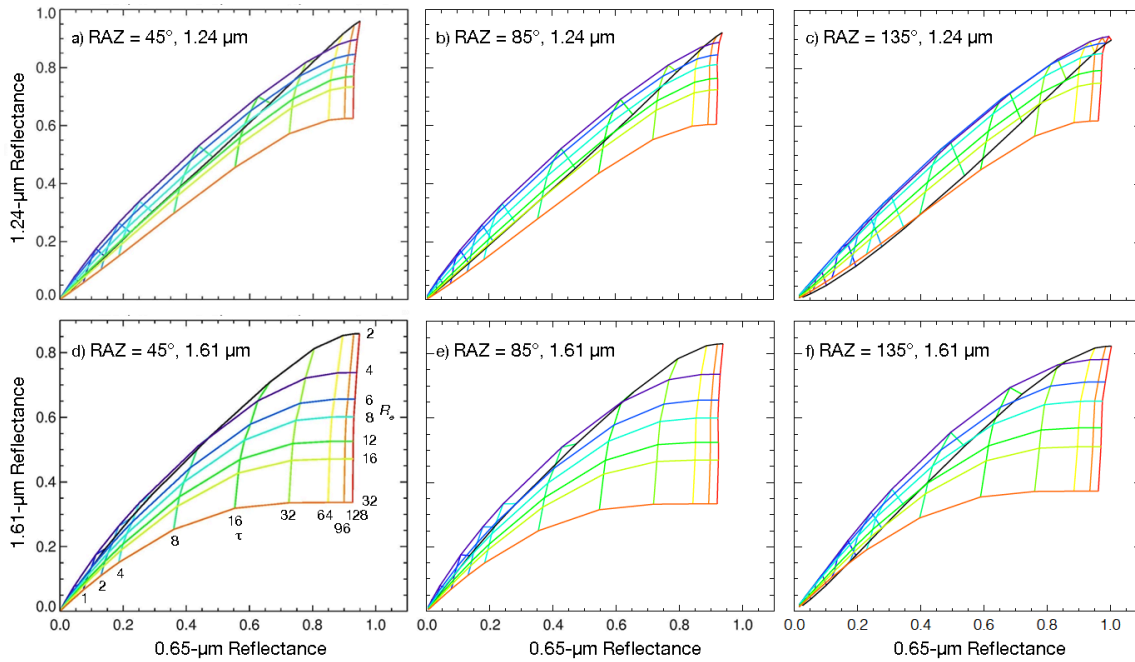
Figure 24.   Model liquid water cloud NIR reflectance versus VIS reflectance from CV1S LUTs at SZA = 45.6°, VZA = 31.8° for range of τ and R_e. Top: 1.24-µm reflectances, Bottom: 1.61-µm reflectances. Left: RAZ = 45°, Center: RAZ = 85°, Right: 135°.
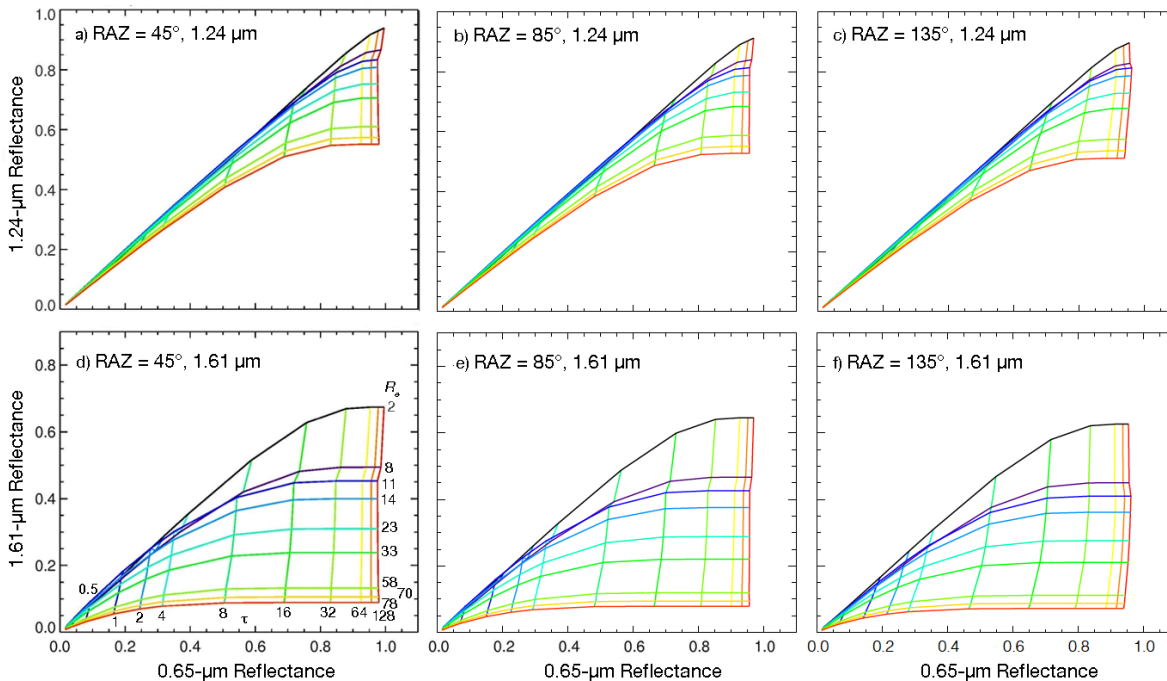

Figure 25. Same as Figure 24, except for ice clouds.

The behavior of the ice-cloud curves (Figure 25) is quite similar, but the reduced separation is more extreme at 1.24 µm for $\tau < 8$ (Figure 25a, b, c). This would introduce much greater uncertainty into the ice retrievals, which could help explain the small fraction of retrieved pixels and larger average values for those pixels that were retrieved. The iteration used to solve for R_e and τ simultaneously begins with the largest value of R_e in the LUT. If it finds a solution for a large R_e and the error in the reflectance calculated from the

assumed optical depth does not decrease significantly for a smaller R_e, then the iteration stops. When the reflectance curves are very close or the dependence is not monotonic, the larger R_e value is more likely to be selected. For larger optical depths, the spread in curves is even greater than seen for the water droplet model. This greater spread could explain why the R_e(1.6) results for ice yield a more normal histogram (Figure 23c) than that for R_e(1.6) for water droplets (Figure 22c). Nevertheless, the histogram remains broad and has a mode at 45 μm. That mode drops to 33 μm for higher optical depth range in Figure 23.

From these analyses, it is clear that the R_e determined using reflectances from the alternative wavelengths is quite uncertain if the cloud is thin. A value of $\tau > 6$ is recommended as a conservative threshold for yielding an accurate retrieval for these alternate wavelengths. The exact τ threshold value at either alternative wavelength depends on the phase and the angles and, likely, the surface characteristics. Retrievals at each wavelength correspond to a certain thickness at the top of cloud. As the wavelength increases, the representative thickness decreases. Thus, R_e(3.74) may correspond to the top 3-8 optical depth at cloud top, while R_e(1.24) and R_e(1.60) can represent optical depths as much as 20 - 60 and 10 – 20, respectively, depending on R_e and the viewing and illumination angles (e.g., Chang and Li, 2002). Thus, R_e(1.24) probably provides little additional information about the effective radius, except when τ exceeds 20, the optical depths for which the retrieval is most accurate. Likewise, R_e(1.61) does not provide much additional information about optically thin clouds, which are more suited for 3.74-μm retrievals. Thus, when carefully used, the three retrievals, when available should be valuable for gaining understanding about the cloud vertical structure for optically thick clouds.

Alternate cloud top height:

The BTM, used to provide an alternative estimate of Z_t, is applied only when its retrieved temperature corresponds to a pressure less than 600 hPa. Thus, it is mostly applicable to ice clouds. Figure 26 maps the distributions of 2013 daytime mean cloud-top heights from Aqua CM4 MCAT, CV1S BTM, and the CV1S standard retrieval (Z_t). Overall, the standard retrieval (Figure 26c) yields the highest cloud tops in the nonpolar regions, 10.8 km, on average, compared to CM4A with 9.5 km (Figure 26a) and BTM with 10.5 km (Figure 26b). Over polar regions, the BTM produces the highest cloud tops. Similar results are found at night (not shown). It should be noted that there are some sampling differences among the methods and the BTM result sometimes substitutes for the standard value. Nevertheless, it is clear that there is a discontinuity between the MODIS and VIIRS alternative cloud top height product, which will need to be resolved in future editions.
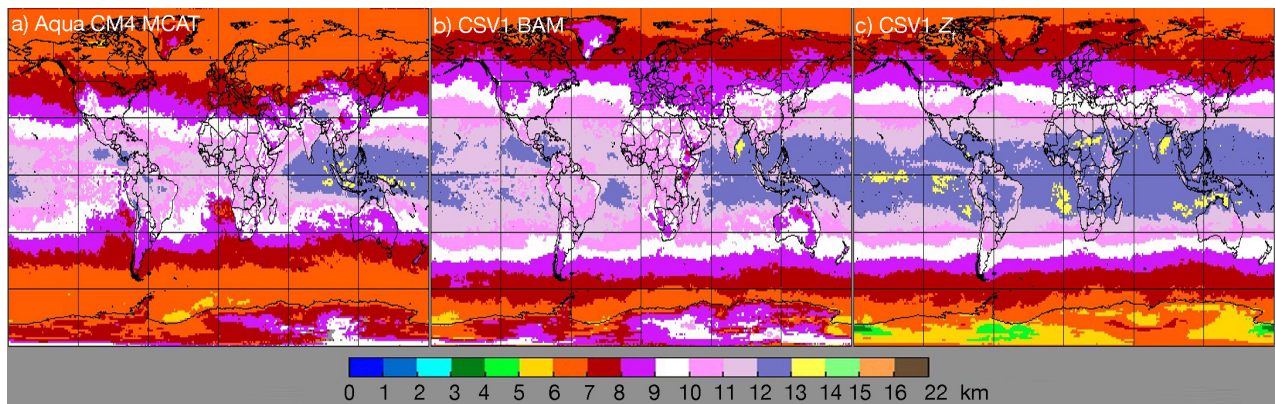

Figure 26.   Mean 2013 cloud-top heights from (a) Aqua CM4 MCAT, (b) CV1S BTM, and (c) CV1S standard retrieval for ice clouds.

Multilayer cloud fraction and layer properties:

The multilayer (ML) identification algorithm for ice clouds over water clouds is applied to every cloudy VIIRS pixel and returns a flag indicating the pixel is multilayer cloud, convective or thick cloud, single-layer (SL) cloud, or clear. Detection and retrieval of the ML cloud parameters relies on the BTM for CV1S and is therefore likely to yield different results than the MCAT used for CM4. Figure 27 compares the multilayer cloud detection fractions for 2013. The daytime CV1S patterns (Figure 27a) are similar to those for Aqua CM4 MCAT retrievals (Figure 27b), but the MCAT detects significantly more ML clouds. At night, the differences between the VIIRS (Figure 27c) and MODIS (Figure 27d) retrievals deepen as the CV1S BTM results drop dramatically while maintaining similar patterns. The CM4A ML fraction only drops slightly. The MCAT relies on the visible optical depth, which is retrieved using the visible channel in sunlit

conditions and the brightness temperature difference during the night. The BTM relies on the same channels, but there is reduced independent information at night because it uses the same channels for both cloud height and optical depth.
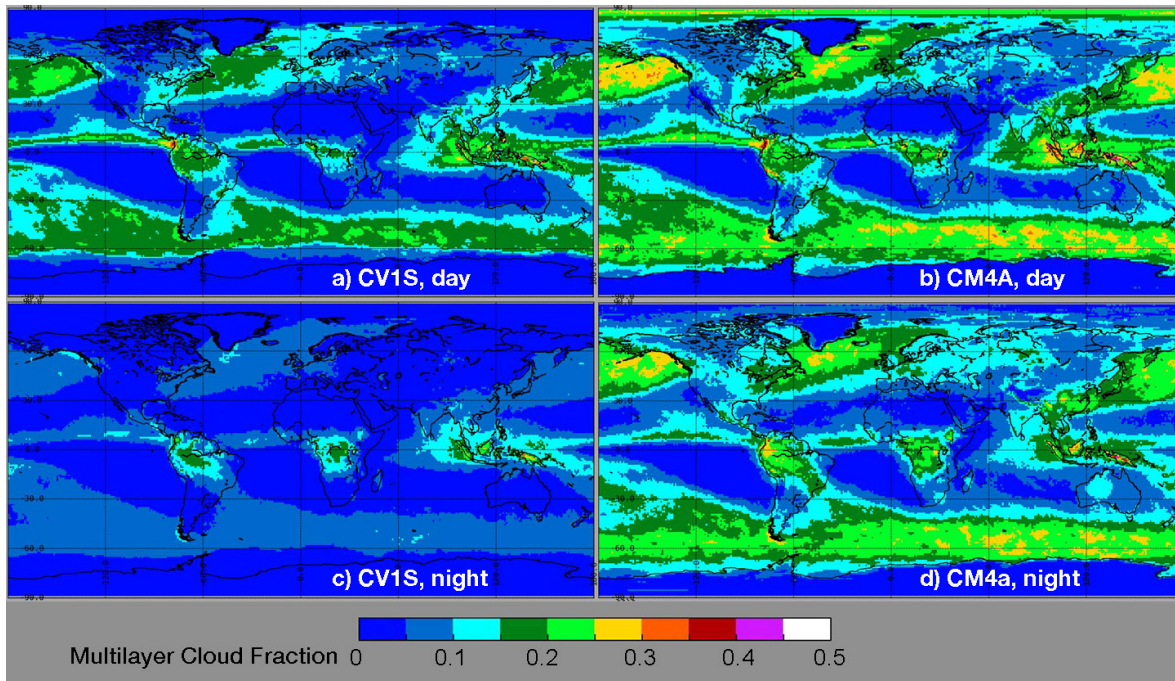

Figure 27.   Mean 2013 daytime multilayer cloud fraction from CERES SNPP VIIRS (left) and Aqua (right) retrievals for day (top) and night (bottom).

Table 10.   Mean multilayer cloud fraction from Aqua Ed4 and SNPP Ed1a, 2013.

	Ocean			Land			Ocean & Land		
	Non-polar	Polar	Global	Non-polar	Polar	Global	Non-polar	Polar	Global
Daytime									
Aqua	0.136	0.164	0.139	0.103	0.046	0.091	0.127	0.110	0.125
SNPP	0.106	0.065	0. 101	0.074	0.028	0.064	0.097	0.048	0.091
Nighttime									
Aqua	0.11	0.157	0.123	0.114	0.069	0.105	0.117	0.117	0.117
SNPP	0.054	0.033	0.052	0.051	0.013	0.043	0.054	0.024	0.050

Overall, the 2013 global daytime ML means from CV1S are roughly 25% less than those for CM4A (Table 10). The differences are smaller in nonpolar zones and greater over polar regions. This lack of polar ML detection is enhanced at night, when the BTM detects 80% fewer ML clouds than the MCAT. Over nonpolar regions, the SNPP ML fraction is only 46% of that from CM4A.

Retrievals of upper and lower-layer cloud top heights and microphysical properties are performed for each pixel identified as multilayered. Figure 28 maps the mean 2013 upper and lower-layer cloud top heights for CM4A (left) and CV1S (right). The CV1S upper cloud heights (Figure 28a) exceed the CV1S means (Figure 28b) everywhere. Conversely, the SNPP lower-layer clouds (Figure 28d) are, on average, lower than their CM4A counterparts (Figure 28c). This is not surprising since, for a given observed brightness temperature, a higher upper cloud will yield a lower low cloud in the height retrievals. Overall, for day and night, the global, polar and nonpolar averages (Table 11) of the upper cloud heights from CV1S are significantly greater than the corresponding CM4A means. The opposite holds true for the lower cloud heights. The global daytime differences in the upper and lower cloud heights are 1.3 km and -0.5 km, respectively. The corresponding nocturnal differences are 2.0 km and -0.6 km. In general, the mean upper cloud heights from both satellites are higher than the ice cloud heights in Table 5. The lower-layer heights are generally lower than the Table 5 water cloud altitudes. It should be noted that the results in Table 5 are for all clouds and will include multilayered clouds that should cause the

water cloud heights to be too high and the ice cloud heights to be too low. Additionally, there are some sampling population differences that can contribute to the differences.

Multilayer infrared optical depth, cloud effective water droplet and effective ice crystal radius are also retrieved for both lower and upper layers, respectively. The multilayer products are considered experimental in both CM4 and CV1S, and are not expected to detect all multilayer clouds, nor to have no false detections. Rather, these products serve as an initial database for exploring the quality of the results, for initial studies of the impact of multilayer clouds on the radiation budget, and for development of more refined methods for multilayer cloud diagnosis and retrieval.
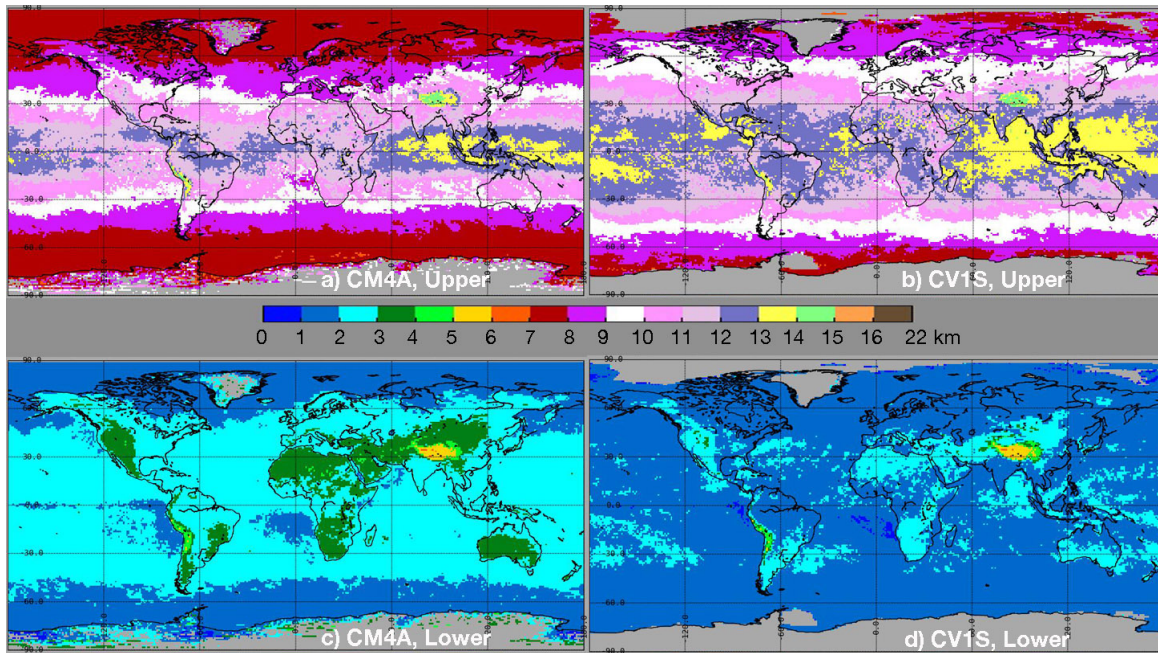

Figure 28.   Same as Figure 27, except for daytime multilayer cloud top height for upper and lower layers.

Table 11.   Mean multilayer cloud top height (km) for upper and lower layers. Aqua Ed4 and SNPP Ed1a, 2013.

	Ocean			Land			Ocean & Land		
	Non-polar	Polar	Global	Non-polar	Polar	Global	Non-polar	Polar	Global
Day									
Aqua (upper)	9.87	7.40	9.57	10.63	7.91	10.35	10.03	7.50	9.73
SNPP (upper)	11.22	8.29	11.03	11.32	8.93	11.10	11.24	8.46	11.05
Aqua (lower)	2.35	1.53	2.25	2.86	2.77	2.01	2.46	1.63	2.36
SNPP (lower)	1.80	1.50	1.78	1.93	1.63	1.91	1.83	1.54	1.81
Night									
Aqua (upper)	8.95	7.27	8.73	9.93	7.77	9.63	9.20	7.40	8.96
SNPP (upper)	10.77	7.62	10.57	11.68	8.36	10.80	11.00	7.80	11.00
Aqua (lower)	2.28	1.58	2.19	2.83	1.84	2.69	2.42	1.65	2.32
SNPP (lower)	1.72	1.46	1.70	1.81	1.33	1.78	1.74	1.43	1.72

Comparison with other measurements

Comparisons of the CV1S results with those from CM4A are valuable for validating the CV1S data because of the required consistency and because a considerable amount of validation has been performed for the CERES MODIS cloud products as reported in Trepte et al. (2019), Minnis et al. (2021), and Yost et al. (2021). Nevertheless, additional comparisons lend more confidence to the quality of the CERES VIIRS cloud properties. Some of these are described below.

Cloud amount:

The CV1S data were compared to CALIOP data for January, April, July, and October (JAJO) 2015 and 2016 to assess the accuracy of several cloud properties including the cloud mask. The CALIOP Vertical Feature Mask (VFM) was used to match the 5-km cloud layers products with the nearest CERES VIIRS pixel retrieval in the same manner as Yost et al. (2021). VIIRS pixels were matched to each of the CALIOP observations if (1) the observation times of the VIIRS pixels were within $\pm$15 minutes of the CALIOP observation times and if (2) the VIIRS pixels were located within 2.5 km of the midpoint of the 5-km CALIPSO track segments. This matching scheme typically results in 1-4 VIIRS pixels matched to each CALIOP observation. When more than one pixel was matched, the mean cloud properties were computed, and if more than one cloud phase was involved the mean properties were computed separately for the water and ice phases. Because CALIOP and VIIRS cloud fractions can have values ranging 0.0 – 1.0, "clear" and "cloudy" labels are ultimately determined by two different methods. In the first method, matches having CALIOP CF < 0.50 are labeled "CALIOP clear" and those having CALIOP CF $\geq$ 0.50 are labeled "CALIOP cloudy". Except as otherwise noted, CALIOP cloud detections using 20-km or and 80-km horizontal averaging were treated as clear sky when computing CALIOP cloud fraction. Likewise, matches having VIIRS CF < 0.50 and VIIRS $\geq$ 0.50 are labeled "VIIRS clear" and "VIIRS cloudy", respectively. In the second method, only those observations having CF = 0.0 were considered "clear", those with CF = 1.0 were considered "cloudy", and those that were partially cloudy were excluded from analysis. The former method, denoted as "50/50" produces results representative of all matches, while the latter method, denoted "0/100", produces results for the subset of matches which are not complicated by partial cloudiness.

The mask comparisons are summarized in Table 12. Combining day and night results, the CV1S cloud mask agrees with CALIOP 91% of the time over all surfaces when considering the 0/100 cases. This agreement decreases to 85% for the 50/50 case. Yet, inclusion of the 50/50 cases has minimal impact on the biases indicating that those partly cloudy cases increase the random error. Agreement is greater over ocean than over land, in general, because of larger uncertainties in the land surface temperatures and reflectivities relative to those for the ocean. Thus, the mask tends to underestimate clouds over land both day and night while being relatively unbiased over ice-free ocean during the day. Over snow/ice-covered areas, the agreement decreases to 90% during the day and 76% at night. The latter number reflects the difficulty of distinguishing clouds from the extremely cold surfaces during the polar night. Cloud amounts over snow/ice surfaces are underestimated by 0.03 and 0.09, on average, during day and night, respectively. These results are very similar to those presented by Trepte et al. (2019). For example, the global fraction correct during the day (night) is 0.932 (0.883) in Table 12 compared to 0.936 (0.881) for CM4A. The magnitude of the CV1S bias and false alarm rates are greater than those for CM4A, especially at night, as might be expected from the earlier comparisons of CV1S and CM4A cloud fractions. It should be noted that the above cloud amount differences are based on assuming that the matched CALIOP and VIIRS footprints are either totally clear or completely cloudy. In reality, there are non-zero cloud amounts in the subset of 50/50 clear pixels absent the 0/100 cases. Likewise, the cloud fractions in that subset are less than unity for the cloudy pixels. The true bias must be measured by comparing the average cloud amounts.

Table 12.   Comparison of CERES SNPP VIIRS Ed1a cloud mask to matched CALIPSO data, JAJO 2015 and 2016.

Day	Fraction Correct 0/100 (50/50)	Bias 0/100 (50/50)	False Alarm Rate 0/100 (50/50)	Hansen-Kuiper Skill Score 0/100 (50/50)	Number of Matches x 10^3 0/100 (50/50)
Land, Snow/Ice-free	0.919 (0.867)	-0.040 (-0.039)	0.038 (0.084)	0.847 (0.738)	405 (524)
Ocean, Snow/Ice-free	0.945 (0.878)	-0.008 (-0.004)	0.032 (0.084)	0.861 (0.707)	1035 (1386)
Snow/Ice-covered	0.902 (0.881)	-0.030 (-0.024)	0.061 (0.080)	0.808 (0.761)	450 (529)
Global, All surfaces	0.929 (0.876)	-0.020 (-0.016)	0.039 (0.083)	0.853 (0.733)	1891 (2440)
Global, All surfaces*	0.932 (0.876)	-0.018 (-0.014)	0.039 (0.083)	0.848 (0.722)	-
Night					
Land, Snow/Ice-free	0.889 (0.855)	-0.023 (-0.014)	0.077 (0.112)	0.779 (0.705)	394 (488)
Ocean, Snow/Ice-free	0.934 (0.870)	-0.031 (-0.040)	0.021 (0.061)	0.828 (0.685)	1040 (1462)
Snow/Ice-covered	0.764 (0.734)	-0.091 (-0.078)	0.130 (0.164)	0.542 (0.468)	796 (945)
Global, All surfaces	0.867 (0.823)	-0.050 (-0.048)	0.060 (0.098)	0.721 (0.621)	2194 (2895)
Global, All surfaces*	0.883 (0.832)	-0.045 (-0.046)	0.058 (0.078)	0.746 (0.632)	-

* Calculated as a linear combination of the different surfaces using more representative weighting than the number of samples.

Cloud phase:

Cloud phase was validated by comparing the phase selections from CV1S to those from CALIOP using two different sets of matches. The first set includes only matches determined by CALIOP to have overcast, SL, single-phase clouds and represents a subset of matches for which validation metrics are expected to be very favorable. The second set includes all matches in the first set but also includes overcast matches with multiple cloud layers and in some cases both phases or even "unknown" phase. In cases involving more than one phase, the predominant phase of the uppermost layer was ultimately chosen as the CALIOP cloud phase to use for the following analyses. This set includes more data but there is also somewhat less confidence in the assigned phase due to the presence of both phases or "unknown" phase in some of the CALIOP profiles. Validation metrics for this category are expected to be less favorable but give a more comprehensive understanding of all the complex cloud systems encountered. Table 13 presents results for both sets of matches. Results for the second set are given in parentheses. The first set of cases represents about 51% of overcast matches over the globe, while the second accounts for > 99%. Over snow/ice-free land and ocean, the agreement is 92 and 96%, respectively, during the day for SL cases. The fractional agreement drops to 80 and 85%, respectively, for all overcast cases. Over snow-covered surfaces, the agreement is similar to that over land, though the ice false alarm rate (FAR) is greater, while the water FAR is larger for snow-free land. Globally, ice and water FARs differ by only 0.01, however, the water cloud amount is nearly double the ice amount, so the amount of false liquid SL clouds will almost be twice that for ice. For the second category, the ice FARs increase by 0.017, on average, but jump by 0.165 for water clouds, indicating that a significant portion of multi-layer clouds are classified are denoted as a water by CV1S.

The impact of the phase errors is evident in the zonal means plotted in Figure 29. Except for areas south of 65°S, CV1S tends to identify more pixels as liquid than CALIOP (Figure 29a). The differences with CALIOP are greater (less) than those between Aqua and CALIOP (Figure 29c from Yost et al., 2021) in the midlatitudes (tropics), while overall, they are about equal. For ice clouds, CV1S cloud amount is less than CALIOP everywhere except south of 65°S (Figure 29b). The underestimates are worse than those for CM4A everywhere except in the tropics (Figure 29d). For the globe as a whole, the CV1S ice cloud amount is 0.073 less than CALIPSO for 5-km data compared to 0.068 for CM4A.

At night, the agreement over ocean is only slightly less than that during the day (Table 13), but it drops by 0.038 and 0.108 for the SL cases over land and snow/ice covered areas. Globally, the ice cloud FAR is 0.170 at night compared to 0.059 during the day. This rise coincides with a reduced water cloud FAR of only 0.031, suggesting that the error at night favors ice clouds. CV1S water cloud fraction

is underestimated at night in the midlatitudes, but equal to that of CALIOP in the tropics (not shown). Overall, the CV1S liquid amount is 0.062 less than it global CALIOP counterpart. Conversely, CV1S ice cloud amount is slightly less than the CALIOP mean in the tropics, nearly equal in the midlatitudes and greater than CALIOP poleward of 60° latitude (not shown). The VIIRS global mean is 0.005 higher than the average from CALIOP 5-km data.

To determine the source of the differences, the matched data were categorized according to CALIOP cloud phase and layering characteristics (see abscissa of Figure 30). Single-layer clouds with no phase ambiguity were categorized as "single-layer water" or "single-layer ice". SL clouds involving more than one phase or even "unknown" phase were categorized according to the predominant
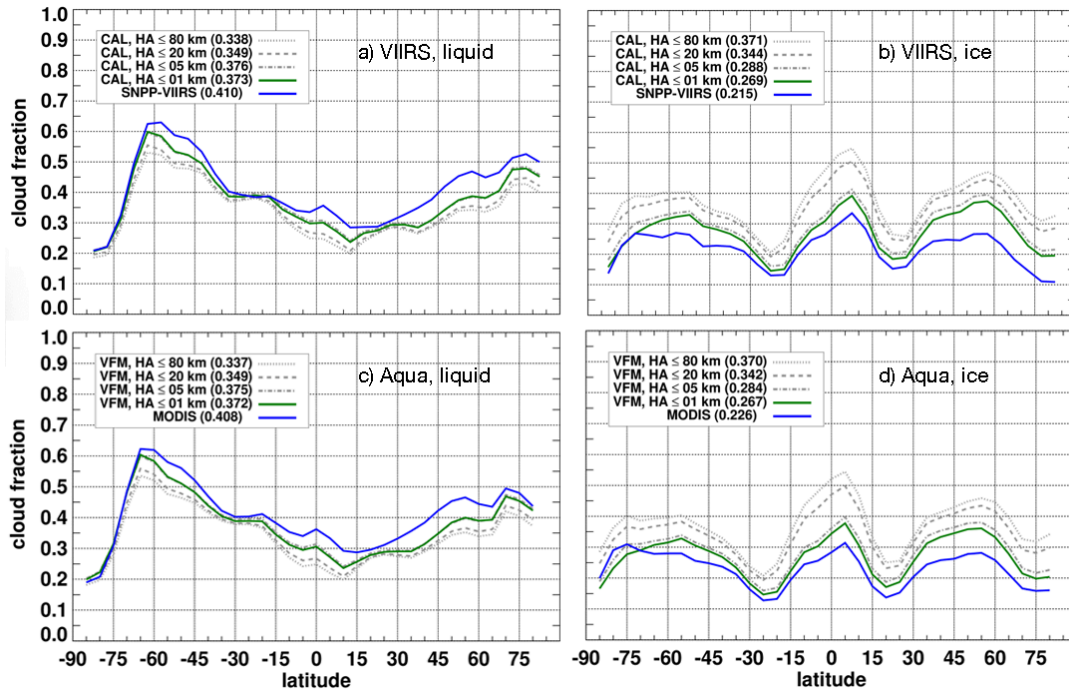

Figure 29.   Daytime zonal cloud amount by cloud-top phase from CALIPSO and matched CV1S (top) and CM4A (bottom) pixels, JAJO 2015-2016.

phase as either "SL water-dominant" or "SL ice-dominant". Multi-layer clouds were categorized according to the phase of the uppermost cloud layer. Matches identified as non-opaque cirrus over low-level water clouds were categorized separately for further analysis but were ultimately considered as ice clouds since the uppermost layer was cirrus. A small number of matches were left unclassified due to logical exceptions or to complete lack of phase information from CALIOP. Each CALIOP category was subdivided according to the CV1S scene classification, i.e., clear, water cloud, ice cloud, or cloudy but no phase retrieval, as shown by the legend in Figure 30. For example, the CALIOP clear classification during the day (Figure 30a) had 606,870 pixels. Of those, CV1S classified 92% as clear, 4% as water cloud and 3% as ice cloud. At night (Figure 30b), the correct clear drops to 85%, while the false ice cloud amount is twice the false liquid amount. An examination of the chart indicates that most of the matches incorrectly classified as liquid cloud by CV1S during the day involve non-opaque cirrus over low-level liquid cloud, while at night, the ice cloud overestimate is due to misclassification of SL water clouds and clear pixels. As a greater part of the overestimate occurs in the polar regions at night, the result is not surprising. Most of the polar water clouds are supercooled and it is difficult to distinguish clear from cloudy scenes in low thermal contrast situations. These results are similar to those for CM4A.

Yost et al. (2021) found that ML systems with very thin ice clouds above a low liquid cloud were very likely to be identified a liquid cloud by CV1S. As the optical depth of the upper cloud, τ_u, increases, the probability of classifying the system as an ice cloud rises. For CM4A, ice phase outcomes were more likely than the liquid phase for $\tau_u > 0.9$ and $\tau_u > 0.3$ for CM4A for day and night, respectively. This difference in τ_u is the result of the spectral channel complements used in the day and night algorithms. Similar results were found for CV1S (not shown). This discrepancy in τ_u explains why the classification of ML clouds as water is double that at night.
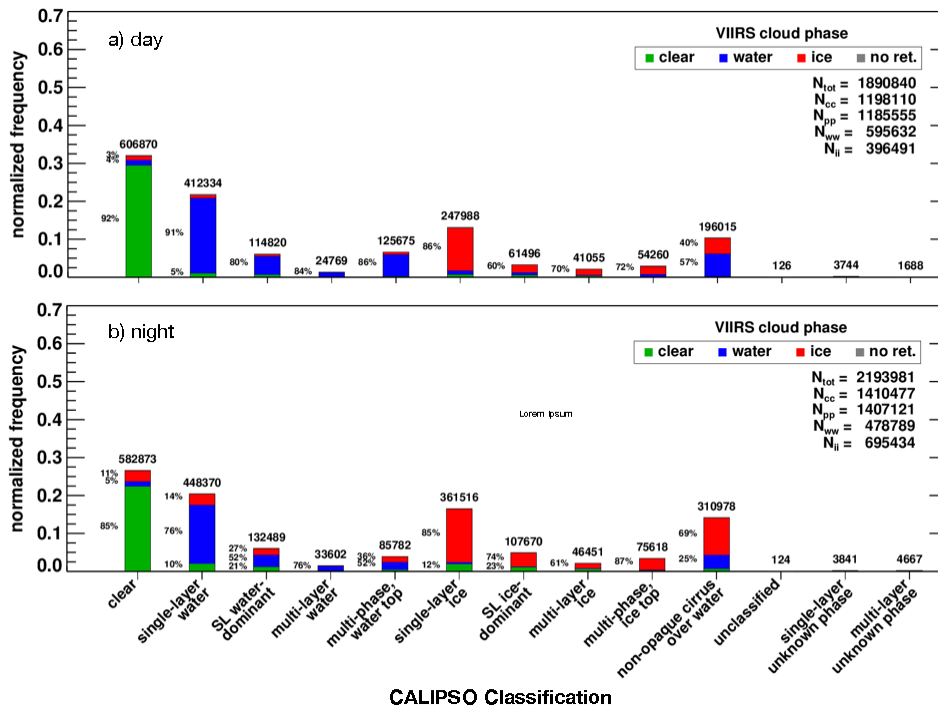
Figure 30.   CV1S scene classification as functions of CALIOP scene classification for JAJO 2015-2016.

The mean nonpolar retrievals of ice and liquid cloud phase amounts from CV1S are close to those determined from VIIRS by the MODIS Atmospheres Science Team (MAST). Platnick et al. (2021) report that the daytime MAST 2012-2020 ice and liquid phase fractions from VIIRS are ~0.24 and ~0.40, values that are within ±0.005 of the same amounts from CV1S.

Cloud height, pressure, and temperature:

The differences in cloud-top heights between CV1S and CALIOP are summarized in Table 13-Table 15 for the 0/100 cases (i.e., overcast pixels). These were computed in the same manner as Yost et al. (2021) where the CALIOP cloud-top is taken as the top of the highest layer in the pixel. Included in the tables are the mean differences, standard deviation of the differences (SDD), and the linear correlation coefficients R between the two heights. For SL-only liquid-water clouds (Table 13), the biases are very close to 0.00 km over all snow/ice-free surfaces during the day. Over snow/ice regions the bias is 0.08 ± 0.94 km. Overall, the bias is 0.02 ± 0.88 km with R = 0.84. At night, Z_t is overestimated by 0.21 km over ice-free ocean and snow/ice-covered surfaces and by 0.14 km over snow- free land. If all clouds with liquid-top layers are considered, the daytime bias is -0.35 ± 1.29 km over ocean and for all surfaces is -0.33 ± 1.35 km. Globally, the mean difference at night for all liquid cases is -0.07 ± 1.14 km. During the day, the heights for altocumulus and altostratus tend to be underestimated, but at night they are too high. This day-night switch could partially explain why the magnitudes of the biases are smaller at night.

Table 13.   Differences between CERES SNPP VIIRS Ed1a and CALIOP cloud top heights for all overcast liquid clouds identified by CALIOP, JAJO 2015 and 2016. Biases are computed as VIIRS – CALIOP.

Day	Single Layer Only			All layering with dominant liquid top		
	Bias (SDD) [km]	R	Number of Matches x 10^{-3}	Bias (SDD) [km]	R	Number of Matches x 10^{-3}
Ocean, Snow/Ice-free	0.00 (0.80)	0.86	259.1	-0.35 (1.29)	0.77	385.0
Land, Snow/Ice-free	-0.01 (1.00)	0.86	40.3	-0.42 (1.40)	0.77	82.7
Land & Ocean, Snow/Ice-covered	0.08 (0.94)	0.81	74.6	-0.23 (1.29)	0.68	127.9
All surfaces	0.02 (0.85)	0.77	374.0	-0.33 (1.31)	0.77	595.6
Night						
Ocean, Snow/Ice-free	0.21 (0.73)	0.79	265.7	-0.05 (1.12)	0.72	362.3
Land, Snow/Ice-free	0.14 (1.23)	0.87	31.4	-0.22 (1.27)	0.79	53.9
Land & Ocean, Snow/Ice-covered	0.21 (0.85)	0.70	42.6	-0.01 (1.06)	0.61	62.5
All surfaces	0.20 (0.76)	0.82	339.8	-0.07 (1.14)	0.75	478.8

The daytime SL biases in Table 13 are similar to those for CM4A (Yost et al. 2021), but the SDDs are slightly greater, possibly as a result of the larger time window used for matching the data. However, on average, the nocturnal differences and SDDs for CV1S are larger than their CM4A counterparts for SL clouds. For all pixels classified as water clouds, the daytime biases are close to those from CM4A, while at night the CV1S differences are slightly improved over those from Aqua.

Table 14 lists the mean differences and associated statistics for non-opaque ice clouds, which typically have $\tau < 5$. During the day over ice-free ocean, the CV1S underestimates the SL CALIOP cloud-top height, Z_t(CA), by 1.28 km, an 0.8 km drop from CM4A difference. Over land and snow/ice surfaces, the difference decreased by 0.5 km and 0.8 km, respectively, relative to the analysis of Yost et al. (2021). The SDDs are also smaller for the CV1S retrievals, 2.09 km down from 2.59 km. The reason for this improvement is not entirely clear, but may be due to the use of the BTM instead of the MCAT to adjust ice cloud heights when the alternate estimate of Z_e was significantly greater than the value from the VISST retrieval. This discrepancy needs further evaluation. For all ice clouds and surfaces, Z_t(V) – Z_t(CA) is -1.22 ± 2.16 km, a value only slightly greater in magnitude than for SL clouds. This difference can be compared to the

Table 14.   Differences, SNPP VIIRS Ed1 – CALIOP, cloud top heights for non-opaque ice clouds, JAJO 2015 and 2016.

Day	Single Layer Only			All layering with ice top		
	Bias (SDD) [km]	R	Number of Matches x 10^{-3}	Bias (SDD) [km]	R	Number of Matches x 10^{-3}
Ocean, Snow/Ice-free	-1.28 (2.12)	0.53	36.7	-1.34 (2.20)	0.64	68.2
Land, Snow/Ice-free	-0.68 (1.93)	0.59	14.7	-0.85 (2.17)	0.64	26.5
Land & Ocean, Snow/Ice-covered	-1.40 (2.08)	0.54	12.3	-1.25 (2.00)	0.55	29.7
All surfaces	-1.17 (2.09)	0.71	63.7	-1.22 (2.16)	0.76	124.4
Night						
Ocean, Snow/Ice-free	-0.47 (2.00)	0.66	57.1	-0.86 (2.34)	0.71	156.9
Land, Snow/Ice-free	-0.22 (2.08)	0.66	33.2	-0.57 (2.34)	0.69	60.7
Land & Ocean, Snow/Ice-covered	-1.30 (2.18)	0.43	68.6	-0.89 (2.35)	0.46	163.9
All surfaces	-0.77 (2.14)	0.76	158.9	-0.83 (2.35)	0.76	381.5

Table 15.   Differences, SNPP VIIRS Ed1 – CALIPSO, cloud top heights for opaque ice clouds, JAJO 2015 and 2016.

Day	Single Layer Only			All layering with ice top		
	Bias (SDD) [km]	R	Number of Matches x 10^{-3}	Bias (SDD) [km]	R	Number of Matches x 10^{-3}
Ocean, Snow/Ice-free	-0.90 (1.28)	0.86	101.4	-1.24 (1.61)	0.84	181.5
Land, Snow/Ice-free	-0.58 (1.30)	0.84	35.7	-0.94 (1.59)	0.82	57.6
Land & Ocean, Snow/Ice-covered	-0.79 (1.35)	0.61	12.5	-1.06 (1.55)	0.61	33.0
All surfaces	-0.81 (1.30)	0.86	149.7	-1.16 (1.60)	0.84	272.1
Night						
Ocean, Snow/Ice-free	-0.45 (1.34)	0.86	86.6	-0.84 (1.79)	0.80	180.5
Land, Snow/Ice-free	-0.51 (1.51)	0.82	28.6	-1.13 (2.09)	0.74	54.9
Land & Ocean, Snow/Ice-covered	-0.92 (1.72)	0.61	33.2	-1.03 (1.86)	0.59	78.4
All surfaces	-0.57 (1.48)	0.85	148.3	-0.94 (1.87)	0.80	313.9

mean of -1.87 ± 2.54 km from CM4A. Note, the correlation coefficients are around 0.55 and 0.64 for SL clouds when the different surfaces are considered separately. When combined, R increases to 0.71, presumably because the combined data provide a greater range of heights. A similar increase was found for all non-opaque cirrus clouds. The magnitudes of the differences in the CV1S non-opaque ice cloud top heights are smaller at night (Table 14, bottom), with an overall mean of -0.77 ± 2.14 km. This represents an improvement of 0.2 km in the bias over the CM4A results. If all ice clouds are considered, the differences are -0.83 ± 2.35 km, only slightly greater in magnitude than the SL case. Yost et al. (2021) found a difference of -1.31 ± 3.07 km for CM4A. It can be concluded that the CV1S top heights for non-opaque ice clouds are more accurate than their CM4A counterparts for both day and night.

Opaque ice cloud-top height differences are listed in Table 15. For SL clouds, $|Z_t(V) - Z_t(CA)| < 1.00$ km for all surfaces day and night. On average, it is -0.81 ± 1.30 km during the day and -0.57 ± 1.48 km at night. For all cases together, the underestimate is larger, -1.16 ± 1.60 km and -0.94 ± 1.87 km during the day and night, respectively. The magnitudes of daytime differences are similar to those from CM4A (corrected top in Table IV of Yost et al. 2021). The nocturnal magnitudes, however, are smaller than their CM4A counterparts. Surprisingly, the opaque ice cloud height biases are not too different from those for the non-opaque clouds, except for daytime SL clouds which see a reduction of ~0.4 km in the bias. The nocturnal, non-opaque height underestimates are actually smaller than the opaque cloud values at night for the all-layering case. Despite the relatively small differences in the biases, the non-opaque SDDs are significantly larger than their opaque counterparts for both SL-only and all ice cloud cases.

In the comparisons above, only matched data for which CV1S and CALIOP reported the same cloud-top phase were considered. Thus, for the cases when ice clouds were mistakenly identified as liquid water clouds by CV1S, and vice versa, there are likely greater errors in the retrieved cloud-top heights. To determine the uncertainty in Z_t for all clouds regardless of phase accuracy, $Z_t(V) - Z_t(CA)$ was computed for all matched VIIRS and CALIPSO cloudy pixels. Histograms of the differences and the relevant statistics are given in Figure 31 for clouds over all surfaces. Both 50/50 and 0/100 cases are included for completeness. The latter is a subset of the former. Three probability distributions are shown in each graph: all clouds (gray), clouds with $Z_t(CA) \leq 5$ km (blue curve), and clouds with $Z_t(CA) > 5$ km (red).
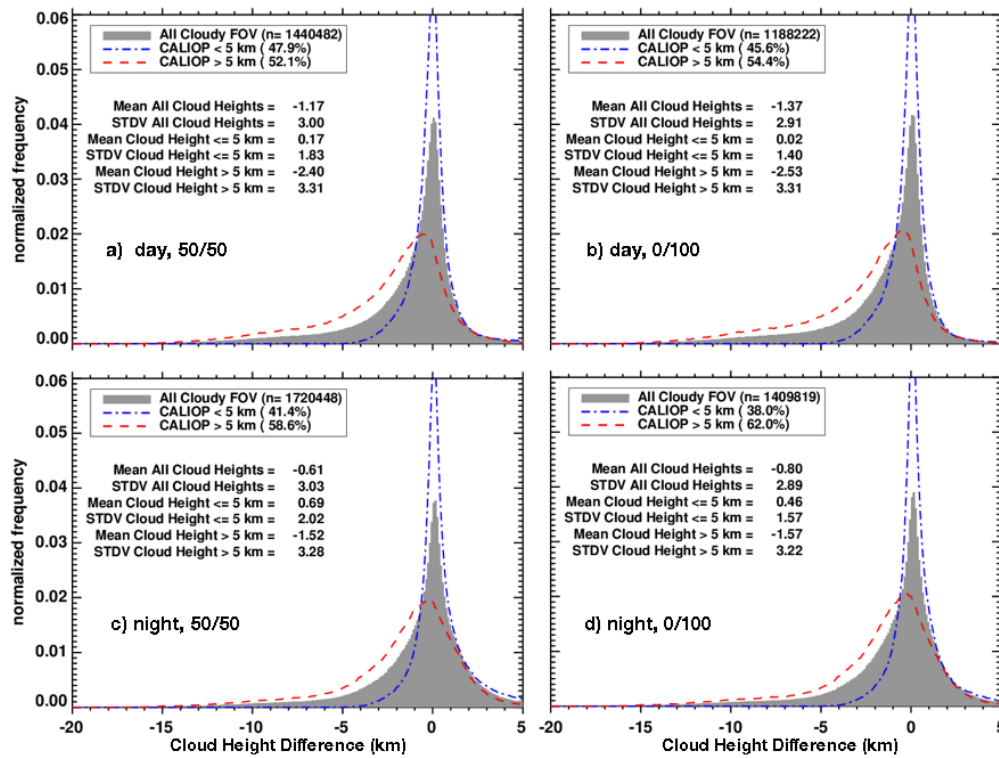
Figure 31.   Histograms of $Z_t(V) - Z_t(CA)$ over the globe for JAJO 2015-2016.

For the lower clouds, the average daytime differences are 0.17 ± 1.83 km and 0.02 ± 1.40 km for 50/50 (Figure 31a) and 0/100 (Figure 31b) cases, respectively. The corresponding biases for the higher clouds are much greater in magnitude: -2.40 ± 3.31 km and -2.53 ±3.31 km. These larger biases and SDDs are primarily due to the inclusion of clouds with mismatched phases and other constraints. For example, the results given for daytime all layer clouds in Table 13-Table 15 account for only 65% of the pixel matches in Figure 31b. Despite the large standard deviations, the biases remain small for low clouds. At night, the lower cloud heights are overestimated by 0.69 ± 2.02 km and 0.46 ± 1.57 km for the 50/50 (Figure 31c) and 0/100 (Figure 31d) constraints, respectively. The greater uncertainty at night is expected because of the reduced amount of information available compared to daytime.

Because of similarities in the CV1S and CM4A optical depths, the VIIRS cloud base height and thickness uncertainties are expected to be similar to the those from Yost et al. (2021), who used matched CERES Ed4 MODIS and CALIOP and CloudSat products for the assessment.

Cloud optical depth, effective particle size, and water path

The standard cloud optical depth, particle effective radius, and water path products from CM4 and CM2 (CERES MODIS Edition 2) have all been evaluated against various surface and airborne observations as discussed by Minnis et al. (2011b, 2021). It is expected that those evaluations are applicable to the CV1S data, except for some slight differences. For example, since $R_e(V) < R_e(M)$ for VISST retrievals of R_e, the biases in liquid water R_e found in some comparisons of CM4 retrievals with other data (e.g., Xi et al., 2014; Dong et al., 2016; Painemal et al., 2016, 2021; Zhang et al., 2017; Minnis et al. 2021) will be reduced slightly because of the smaller values retrieved from VIIRS.

On average, the microphysical properties are similar to those from other observations. The MAST 9-y average nonpolar estimates of R_e from the VIIRS 3.74-μm channel are ~14.2 μm and ~23.0 μm for liquid and ice water, respectively. These means can be compared to the corresponding CV1S averages from Table 7: 12.9 μm and 26.3 μm. The differences maybe due to discrepancies in sampling as only 70% of the pixels identified as liquid water by the MAST algorithms had a retrieval of $R_e(3.74)$. For $R_e(1.61)$, the MAST analysis yields means of ~14.5 μm and ~30.3 μm for liquid and ice, respectively, compared to 15.9 μm and 31.9 μm from CV1S. The larger CERES value for liquid is due primarily to differences in indices of refraction used by the two algorithms. Also, for ice particularly, there may be differences in the optical properties of the assumed ice crystal models used for the LUTs.

32

While the cloud optical depths may not be directly comparable since Platnick et al. (2021) only report means for overcast pixels and there are the aforementioned sampling differences, the MAST VIIRS and CV1S averages are not altogether different. The former yields τ means of ~12.3 for ice and ~13.5 for liquid clouds compared to 11.8 and 13.7, respectively, from Table 6.

As a further check on the consistency with CM4A, the CV1S optical depths are compared with those derived from the CALIOP measurements as in Yost et al. (2021). Figure 32 plots the results for ice-free ocean surfaces for SL cirrus clouds as determined from CALIPSO data. During the day, the CV1S mean is 51% greater than its CALIOP counterpart (Figure 32a). This represents a diminishment
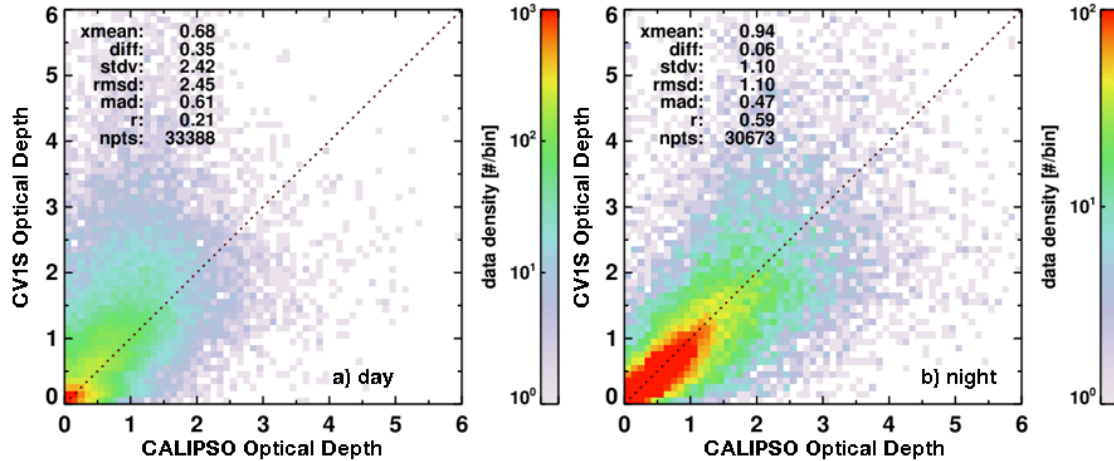

Figure 32.   Comparison of single-layer cirrus optical depths from CV1S and CALIOP, JAJO 2015-2016, over ice-free ocean.

in the value 43% found for CM4A (*ibid*). At night, however, the bias diminishes significantly for both CV1S (Fig. 32b) and CM4A (*ibid*). The former mean is 6% higher than the CALIOP average compared to 5% for the latter.

Validation of the CERES products is a continuing effort. The results presented here are initial assessments of the results. Future studies will attempt to shed more light on the quality of the SNPP VIIRS Ed1a data cloud products and should lead to improvements in the next edition.

Concluding Remarks

The goal of CERES is to develop and use cloud and radiation datasets that are consistent across platforms and instruments. In many respects, the initial cloud properties derived from analysis of the SNPP VIIRS radiances, referred to here as CSV1, are consistent with their CERES Ed4 Aqua MODIS, or CM4A, counterparts. The trends in the averages of a given parameter are generally the same except for those parameters affected by calibration changes such as the switch from MODIS Collection 5 to Collection 6.1, which affected some of the thermal infrared channels, or the change in the source for the VIIRS data that altered some of the solar channel calibrations. Other differences in mean values can be explained by changes in cloud reflectance models, resolution differences, and an unrepresentative solar constant value for the VIIRS 3.8-μm channel. Still other issues causing differences are lack of certain channels on VIIRS that were used by MODIS for phase selection over polar regions. Data users should be cautious when employing the polar cloud optical depths from both VIIRS and MODIS, as they are likely overestimated in many cases, particularly for liquid water clouds. It is not clear how much the current inconsistencies between the two datasets affect the radiative fluxes derived from the application of the cloud properties to their determination.

The biases in the CV1S cloud detection relative to the CM4A parameters are confirmed by the CALIPSO comparisons. Despite the biases, the CV1S cloud detection yields nearly the same fraction of correct scene identifications as CM4A relative to the CALIPSO data. The accuracies of the CV1S cloud phase and top heights relative to the CALIPSO values are also quite similar to their CM4A counterparts. Except for the cloud fraction biases, the CV1S and CM4A retrievals are equally reliable for the parameters evaluated with the CALIPSO cloud properties.

Improvement of the consistency between the MODIS and VIIRS retrievals will require additional research and analysis that should lead to changes in the analysis algorithms and input data for the detection and retrieval systems for both instruments. Normalization of

the calibrations is a crucial first step. Improvement of the VIIRS scene identification scheme to detect more clouds, especially at night, is also a key component of any revision. To improve the retrieval of cloud optical depth over snow and ice, it is recommended to use a near-infrared channel other than 1.24 μm for clouds that are not optically thick. The 1.24-μm snow reflectances are highly variable and much greater than those at the 2.13 and 1.61-μm wavelengths and thus is more susceptible to uncertainties in the clear-sky albedos. Better phase detection could be accomplished if multilayer clouds could be confidently detected. They often yield a liquid water determination of cloud-top phase for optically thin ice clouds over lower water clouds. The current methods employed experimentally here have not yet been proven reliable. Retrievals of cloud effective particle sizes using near-infrared channels should be limited to optical depth ranges that yield singular solutions and have sensitivity of particle size to non-negligible changes in reflectance. These suggested improvements and others should enhance the consistency and accuracy of future CERES cloud datasets. In the meantime, the CERES SNPP VIIRS Ed1a cloud properties should be quite useful for cloud and radiation analyses, particularly when the differences relative to the MODIS datasets are known and taken into account.

Return to Quality Summary for: SSF S-NPP Edition2A .

References

Bennartz, R., 2007: Global assessment of marine boundary layer cloud droplet number concentration from satellite. *J. Geophys. Res.*, **112**, D02201, doi:10.1029/2006JD007547.

Chang, F.L., and Z. Li (2002), Estimating the vertical variation of cloud droplet effective radius using multispectral near-infrared satellite measurements. *J. Geophys. Res.* 107, NO D15, 10.1029/2001JD000766

Chang, F.-L., P. Minnis, B. Lin, M. Khaiyer, R. Palikonda, and D. Spangenberg, 2010a: A modified method for inferring cloud top height using GOES-12 imager 10.7- and 13.3-μm data. *J. Geophys. Res.*, **115**, D06208, doi:10.1029/2009JD012304.

Chang, F.-L., P. Minnis, J. K. Ayers, M. J. McGill, R. Palikonda, D. A. Spangenberg, W. L. Smith, Jr., and C. R. Yost, 2010b: Evaluation of satellite-based upper-troposphere cloud-top height retrievals in multilayer cloud conditions during TC4. *J. Geophys. Res.*, D00J05, **115**, doi:10.1029/2009JD012800.

Chang, F.-L., P. Minnis, S. Sun-Mack, L. Nyugen, and Yan Chen, 2010c: On the satellite determination of multi-layered multi-phase cloud properties. *Proc. AMS 13th Conf. Atmos. Rad. and Cloud Phys.*, Portland, OR, June 27 – July 2, JP1.10. https://ams.confex.com/ams/13CldPhy13AtRad/webprogram/Paper171180.html

Dong, X. and P. Minnis, 2022: Chapter 8: Stratus, stratocumulus, and remote sensing, In *Fast Physics in Large Scale Atmospheric Models: Parameterization, Evaluation, and Observations*, Y. Liu, P. Kollias, and L. Donner, Eds., AGU-Wiley Publ., in press.

Dong, X., B. Xi, S. Qiu, P. Minnis, S. Sun-Mack, and F. Rose, 2016: A radiation closure study of Arctic stratus cloud microphysical properties using the collocated satellite-surface data and Fu-Liou radiative transfer model. *J. Geophys. Res.*, **121**, doi:10.1002/2016JD025255.

Lee, T. F., S. D. Miller, F. J. Turk, C. Schueler, R. Julian, S. Deyo, P. Dills, and S. Wang, 2006: The NPOESS VIIRS day/night visible sensor. Bull. Amer. Meteor. Soc., 87, 191–199.

Minnis, P., K. Bedka, Q. Trepte, C. R. Yost, S. T. Bedka, B. Scarino, K. Khlopenkov, and M. M. Khaiyer, 2016: A consistent long-term cloud and clear-sky radiation property dataset from the Advanced Very High Resolution Radiometer (AVHRR). *Climate Algorithm Theoretical Basis Document (C-ATBD), CDRP-ATBD-0826 AVHRR Cloud Properties - NASA*, NOAA CDR Program, 19 September, 159 pp.,   DOI:10.7289/V5HT2M8T.   Available   at https://www1.ncdc.noaa.gov/pub/data/sds/cdr/CDRs/AVHRR_Cloud_Properties_NASA/AlgorithmDescription_01B-30b.pdf

Minnis, P., L. Nguyen, R. Palikonda, P. W. Heck, D. A. Spangenberg, D. R. Doelling, J. K. Ayers, W. L. Smith, Jr., M. M. Khaiyer, Q. Z. Trepte, L. A. Avey, F.-L. Chang, C. R. Yost, T. L. Chee, and S. Sun-Mack, 2008b: Near-real time cloud retrievals from operational and research meteorological satellites. *Proc. SPIE 7107, Remote Sens. Clouds Atmos. XIII*, Cardiff, Wales, UK, 15-18 September, pp. 710703-710703-8, https://doi.org/ 10.1117/12.800344.

Minnis, P., S. Sun-Mack, D. F. Young, P. W. Heck, D. P. Garber, Y. Chen, D. A. Spangenberg, R. F. Arduini, Q. Z. Trepte, W. L. Smith, Jr., J. K. Ayers, S. C. Gibson, W. F. Miller, V. Chakrapani, Y. Takano, K.-N. Liou, Y. Xie, and P. Yang, 2011a: CERES Edition-2 cloud property retrievals using TRMM VIRS and Terra and Aqua MODIS data, Part I: Algorithms. *IEEE Trans. Geosci. Remote Sens.*, **49**, *11*, 4374-4400.

Minnis, P., S. Sun-Mack, Y. Chen, M. M. Khaiyer, Y. Yi, J. K. Ayers, R. R. Brown, X. Dong, S. C. Gibson, P. W. Heck, B. Lin, M. L. Nordeen, L. Nguyen, R. Palikonda, W. L. Smith, Jr., D. A. Spangenberg, Q. Z. Trepte, and B. Xi, 2011b: CERES Edition-2 cloud property retrievals using TRMM VIRS and Terra and Aqua MODIS data, Part II: Examples of average results and comparisons with other data. *IEEE Trans. Geosci. Remote Sens.*, **49**, *11*, 4401-4430, doi:10.1109/TGRS.2011.2144602.

Minnis, P., S. Sun-Mack, C. R. Yost, Y. Chen, W. L. Smith, Jr., F.-L. Chang, P. W. Heck, R. F. Arduini, Q. Z. Trepte, K. Ayers, K. Bedka, S. Bedka, R. R. Brown, E. Heckert, G. Hong, Z. Jin, R. Palikonda, R. Smith, B. Scarino, D. A. Spangenberg, P. Yang, Y. Xie, and Y. Yi, 2021: CERES MODIS cloud product retrievals for Edition 4, Part I: Algorithm changes. *IEEE Trans. Geosci. Remote Sens.*, **59**, 2744-2780, doi:10.1109/TGRS.2020.3008866.

Minnis, P., Q. Z. Trepte, S. Sun-Mack, Y. Chen, D. R. Doelling, D. F. Young, D. A. Spangenberg, W. F. Miller, B. A. Wielicki, R. R. Brown, S. C. Gibson, and E. B. Geier, 2008a: Cloud detection in non-polar regions for CERES using TRMM VIRS and Terra and Aqua MODIS data. *IEEE Trans. Geosci. Remote Sens.*, **46**, 3857-3884.

Minnis, P., C. R. Yost, S. Sun-Mack, and Y. Chen, 2008c: Estimating the physical top altitude of optically thick ice clouds from thermal infrared satellite observations using CALIPSO data. *Geophys. Res. Lett.*, **35**, L12801, doi:10.1029/2008GL033947.

Minnis, P., D. P. Garber, D. F. Young, R. F. Arduini, and Y. Takano, 1998: Parameterization of reflectance and effective emittance for satellite remote sensing of cloud properties. *J. Atmos. Sci.*, **55**, 3313-3339.

Painemal, D., T. Greenwald, M. Cadeddu, and P. Minnis, 2016: First extended validation of satellite microwave liquid water path with ship-based observations of marine low clouds. *Geophys. Res. Lett.*, **43**, doi:10.1002/2016GL069061.

Painemal, D., P. Minnis, and S. Sun-Mack, 2013: The impact of horizontal heterogeneities, cloud fraction, and cloud dynamics on warm cloud effective radii and liquid water path from CERES-like Aqua MODIS retrievals. *Atmos. Chem. Phys.*, **13**, 9997-10003, doi:10.5194/acp-13-9997-2013.

Painemal, D., D. Spangenberg, W. L. Smith, Jr., P. Minnis, B. Cairns, R. H. Moore, and E. Crosbie, 2021: Evaluation of satellite retrievals of liquid clouds from the GOES-13 imager and MODIS over the midlatitude North Atlantic during the NAAMES campaign, *Atmos. Meas. Tech.*, doi:10.5194/amt-2021-7.

Platnick, S., K. Meyer, G. Wind, R. E. Holz, N. Amarasinghe, P. A. Hubanks, B. Marchant, S. Dutcher, and P. Veglio, 2021: The NASA MODIS-VIIRS continuity cloud optical properties products. *Remote Sens.*, **13**, 2, doi:10.3390.rs13010002.

Trepte, Q. Z., P. Minnis, S. Sun-Mack, C. R. Yost, Y. Chen, Z. Jin, F.-L. Chang, W. L. Smith, Jr., K. M. Bedka, and T. L. Chee, 2019: Global cloud detection for CERES Edition 4 using Terra and Aqua MODIS data. *IEEE Trans. Geosci. Remote Sens.*, **57**, 9410-9449, doi:10.1109/TGRS.2019.2926620.

Xi, B., X. Dong, P. Minnis, and S. Sun-Mack, 2014: Comparison of marine boundary layer cloud properties from CERES-MODIS Edition 4 and DOE ARM AMF measurements at the Azores. *J. Geophys. Res.*, **119**, doi:10.1002/2014JD021813.

Xiong, X., et al. (2014), VIIRS on-orbit calibration methodology and performance, *J. Geophys. Res. Atmos.*, 119, 5065–5078, doi:10.1002/2013JD020423.

Yang, P., G. W. Kattawar, G. Hong, P. Minnis, and Y. X. Hu, 2008: Uncertainties associated with the surface texture of ice particles in satellite-based retrieval of cirrus clouds: Part II. Effect of particle surface roughness on retrieved cloud optical thickness and effective particle size. *IEEE Trans. Geosci. Remote Sens.*, **46**(7), 1948-1957, doi:10.1109/TGRS.2008.916472.

Yost, C., P. Minnis, S. Sun-Mack, Y. Chen, and W. L. Smith, Jr., 2021: CERES MODIS cloud product retrievals for Edition 4, Part II: Comparisons to CloudSat and CALIPSO. *IEEE Trans. Geosci. Remote Sens.*, **59**, 3695-3724, doi:10.1109/TGRS.2020.3015155.

Zhang, Z., and S. Platnick (2011). An assessment of differences between cloud effective particle radius for marine water clouds from three MODIS spectral bands. J. Geophys. Res., 116, D20215, doi:10.1029/2011JD016216.

Zhang, Z., X. Dong, B. Xi, H. Song, P.-L. Ma, S. Ghan, S. Platnick, and P. Minnis, 2017: Intercomparisons of marine boundary layer cloud properties from two MODIS products, ground-based retrievals, and a GCM over the ARM Azores site. *J. Geophys. Res.*, **122**, doi:10.1002/2016JD025763.